The Astronomical Journal, 171:72 (18pp), 2026 February https://doi.org/10.3847/1538-3881/ae285b


# Dynamical and Photometric Analysis of NGC 146 and King 14: Evidence for a Comoving, Unbound Cluster Pair

D. Bisht[1], Ing-Guey Jiang[2], W. H. Elsanhoury[3], K. Belwal[1], D. C. Çinar[4], A. Raj[1,5], Shraddha Biswas[1], Arvind K. Dattatrey[6], Geeta Rangwal[7], Devesh P. Sariya[2], Mohit Singh Bisht[1], and Alok Durgapal[8]
[1] Indian Centre For Space Physics 466, Barakhola, Singabari road, Netai Nagar, Kolkata, 700099 West Bengal, India; devendrabisht297@gmail.com, kuldeepbelwal1997@gmail.com
[2] Department of Physics and Institute of Astronomy, National Tsing-Hua University, Hsinchu 30013, Taiwan; jiang@phys.nthu.edu.tw
[3] Physics Department, College of Science, Northern Border University, Arar, Saudi Arabia
[4] Programme of Astronomy and Space Sciences, Institute of Graduate Studies in Science, Istanbul University, Istanbul, 34116, Türkiye
[5] Uttar Pradesh State Institute of Forensic Science (UPSIFS) Aurawan, P.O. Banthra, Lucknow 226401 U.P, India
[6] Indian Institute of Astrophysics, 560034 Bangalore, India
[7] Aryabhatta Research Institute of Observational Sciences, Manora Peak, Nainital 263129, India
[8] Center of Advanced Study, Department of Physics, D. S. B. Campus, Kumaun University, Nainital 263002, India
*Received 2025 October 20; revised 2025 December 2; accepted 2025 December 2; published 2026 January 7*

## Abstract

To understand the nature of the NGC 146–King 14 cluster pair, we conducted a detailed photometric, astrometric, and dynamical study using multiwavelength data from Gaia DR3, Pan-STARRS1, WISE, and TESS. Using a probabilistic approach, we identified 770 and 690 high-probability members of NGC 146 and King 14, respectively. Both clusters exhibit well-defined radial density profiles consistent with King models. We estimate the cluster ages as 20 ± 5 Myr and 50 ± 10 Myr from isochrone fitting, and distances of 2.98 ± 0.33 kpc and 2.51 ± 0.23 kpc from parallaxes after applying the Bailer-Jones criteria. The clusters show consistent mean proper motions. The mass function slopes (1.51 ± 0.18 and 1.50 ± 0.15) are close to the Salpeter value, and the extinction follows a normal Galactic reddening law ($R_V \approx 3.1$). Three-dimensional mapping gives a projected separation of ∼9 pc. Orbit integration using the `galpy` `MWPotential2014` model shows that NGC 146 and King 14 move in nearly circular, disk-like orbits with similar mean orbital radii ($R_m \sim 9$ kpc) and orbital periods of roughly 255 Myr. A dynamical separation of ∼32 pc indicates that both clusters share a common spatial and kinematic association, consistent with a comoving pair. However, their relative velocity exceeds the escape velocity set by their combined mass, indicating they are not gravitationally bound. TESS light curves reveal seven variable stars, including γ Doradus, SPB stars, and eclipsing binaries, though only one is a likely member. Overall, the clusters likely formed within the same giant molecular cloud and now exist as an unbound comoving pair.

*Unified Astronomy Thesaurus concepts:* Stellar kinematics (1608); Open star clusters (1160); Initial mass function (796); Stellar dynamics (1596); Time domain astronomy (2109)

*Materials only available in the online version of record: data behind figure*

## 1. Introduction

Open clusters (OCs) typically contain a few hundred to a few thousand stars formed from a single massive molecular cloud (E. Corsaro et al. 2017). These stars are loosely bound by weak gravitational forces (A. K. Leroy et al. 2018). OCs are valuable for studying the history of star evolution as they originate from the collapse and fragmentation of massive molecular clouds (W. E. Harris & R. E. Pudritz 1994; M. R. Bate et al. 2003). Binary clusters are especially significant among OCs, as they help in understanding the formation, evolution, and characteristics of stars in the Galactic disk (M. Piecka & E. Paunzen 2021). Binary clusters can form when several massive and dense gas clumps within a giant molecular cloud collapse due to gravity. These clumps may give rise to clusters that are nearly the same age and located very close to each other (A. Piatti 2010; B. Arnold et al. 2017; M. D. Mora et al. 2019; R. Darma et al. 2021). Most multiple and embedded clusters quickly disperse or merge due to early disruption (C. J. Lada & E. A. Lada 2003). In some cases, two clusters can become gravitationally bound during a close encounter, forming a binary system with significantly different ages (S. van den Bergh 1996; R. de La Fuente Marcos & C. de La Fuente Marcos 2009). The existence of binary and multiple OCs has been explored for decades. Many studies based on observational data suggested that around 8%–10% of OCs could be genuine binaries (A. Subramaniam et al. 1995; A. Loktin 1997; R. de La Fuente Marcos & C. de La Fuente Marcos 2009). In addition, studies focusing on binary and multiple OCs in the Gaia era are still ongoing, and further investigations are needed in order to fully understand their nature and frequency (F.-F. Song et al. 2023; A. A. Haroon et al. 2024, 2025; Z. Li & Z. Zhu 2025; T. Palma et al. 2025; S. Taşdemir & D. C. Çınar 2025).

The catalog of known OCs continues to expand, and membership determination has become more accurate thanks to the Gaia mission. As a result, the identification of binary clusters has attracted growing interest in recent years. C. Soubiran et al. (2019) identified 21 cluster pairs with small separations; L. Liu & X. Pang (2019) reported 56 candidate

cluster groups based on 3D spatial positions. M. Piecka & E. Paunzen (2021) also identified 60 cluster groupings by examining shared members in low phase-space volumes using the T. Cantat-Gaudin & F. Anders (2020) catalog. These studies highlight the growing potential for discovering new binary cluster systems.

Binary and comoving clusters are essential for understanding star and cluster formation and evolution (J. Casado 2021). They also offer key insights into the mechanisms driving cluster formation and development (E. Dalessandro et al. 2018). They reveal how molecular clouds fragment and how Galactic forces impact cluster survival. Examining unbound or dissolving clusters shows how stars disperse into the field population. These systems also shed light on the Milky Way's past cluster-formation and stellar-migration history (R. Darma et al. 2021; M. Angelo et al. 2022). NGC 146 and King 14 are nearby OCs in the Perseus arm. Their similar distances and proximity have led to discussions of a possible physical connection or a binary nature. The available information for both clusters from the literature is summarized below-

*NGC 146.* NGC 146 (C 0030+630) is an open star cluster located in the constellation of Cassiopeia, approximately 1800 lt-yr away from Earth. It is a relatively young cluster, estimated to be around 40 million years old. NGC 146 contains a mix of late B-type and early A-type stars, which contribute to its brightness. Observational studies, such as those conducted by N. Kharchenko et al. (2005), have focused on the stellar population and overall dynamics of the cluster, uncovering insights into its structure and the impact of the surrounding interstellar medium on its evolution. B. Rojas-Ayala et al. (2010) also studied the relationships between stellar populations and the interstellar environment, highlighting NGC 146 as a target for further astrophysical studies, due to its relatively rich stellar environment.

*King 14.* King 14 (C 0029+628) is an open cluster situated in the constellation of Cassiopeia, approximately 2000 lt-yr from Earth. Characterized as a faint cluster, King 14 has a somewhat dispersed distribution of stars and is estimated to be about 100 Myr old, making it relatively older than others. The cluster consists primarily of F-type stars, with studies emphasizing its membership and stellar content. Research by I. King (1962) provided early observations of the cluster's structure, while W. Dias et al. (2002) investigated its stellar population, shedding light on the characteristics and evolution of older OCs. These studies underscore the challenges posed by King 14's dispersed nature for observational research, yet they remain crucial for understanding the dynamics of such clusters.

The NGC 146–King 14 pair presents a unique case for investigating how young, comoving OCs in the Galactic disk are physically connected and how they evolve dynamically. Studying such pairs is critical, as they serve as laboratories to examine the transition from bound binary clusters to unbound yet kinematically associated systems influenced by Galactic tidal forces. By comparing them, researchers gain insight into the formation of cluster pairs within giant molecular clouds and how their interactions shape the early dynamical evolution. Identifying variable stars within and around these clusters adds further value, since these variables trace recent star formation, stellar pulsations, and possible cluster membership. Analyzing these variables with high-precision TESS photometry deepens understanding of each cluster's stellar population. It provides context for the time-domain evolution and dynamical history of young OCs in the Milky Way.

The primary objective of this study is to investigate whether the OCs NGC 146 and King 14 constitute a physically related or comoving binary cluster system. To address this, we determine their fundamental parameters, examine the mass functions, and analyze their internal kinematics using high-precision Gaia DR3 data. An orbital analysis is conducted to trace their past trajectories and evaluate a possible common origin. Additionally, we employ TESS photometric data to identify and characterize variable stars within and around the clusters. The presence of such variable stars yields insights into the stellar population, ongoing dynamical evolution, and potential field contamination. This comprehensive approach enables us to assess the physical connection, dynamical state, and evolutionary history of the NGC 146–King 14 system within the Galactic disk.

The paper is organized as follows. Section 2 provides a comprehensive description of the datasets employed in this study. Section 3 outlines the methodology used to determine high-probability stellar membership within the clusters. In Section 4, we derive the structural parameters of the clusters, including core and tidal radii. Section 5 presents the estimation of cluster distances from parallax measurements and the determination of their ages through theoretical isochrone fitting. Section 6 examines the dynamical evolution and orbital properties of the clusters. Section 7 investigates the nature of the NGC 146–King 14 pair through their spatial separations and orbital analysis. In Section 8, we perform spectral energy distribution analysis and systematically identify and classify variable stars within the clusters. The key results and implications of our study are discussed in Section 9.

## 2. Data

In this study, we investigate the neighboring OCs NGC 146 and King 14, which exhibit indications of a possible binary or comoving nature. We combine astrometric, photometric, and time-series data from major surveys, including Gaia DR3, WISE, Pan-STARRS1, 2MASS, and TESS, to conduct a comprehensive multiwavelength analysis. This integrated approach allows us to examine the clusters' morphology, spatial distribution, and internal kinematics in detail. Additionally, high-precision TESS photometry enables the detection and characterization of variable stars in the vicinity of these clusters, offering further insights into their stellar content and dynamical evolution.

Figure 1 displays the identification chart and the corresponding stellar surface density map for the region containing the OCs NGC 146 and King 14. The upper panel presents an image from the Digitized Sky Survey (DSS), a publicly available digital collection of astronomical photographs, covering a field of 30′ and highlighting the projected spatial configuration of the two clusters. The circles mark the approximate boundaries of the cluster. The symbols represent the identified variable stars. This chart effectively shows the relative positions and orientations of NGC 146 and King 14 within the observed field. The lower panel illustrates the stellar surface density distribution derived from Gaia DR3 data. The data reveal two distinct and prominent density enhancements corresponding to the centers of NGC 146 and King 14. The smooth transition of the density contours between the clusters

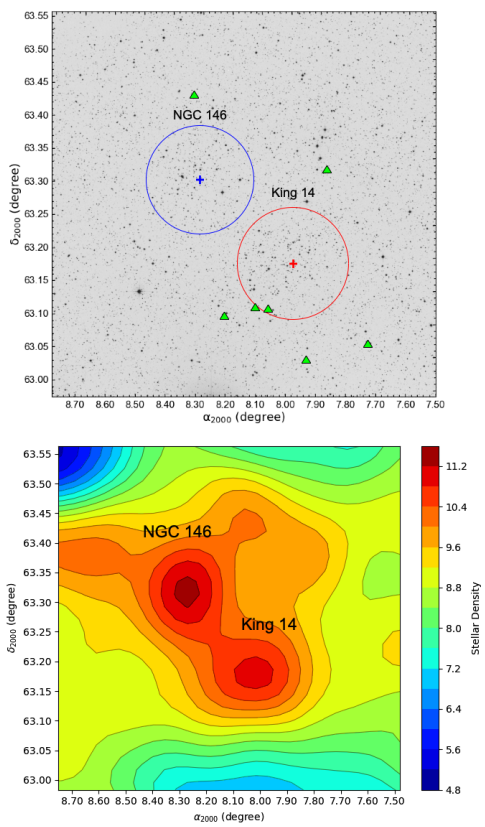


**Figure 1.** Top: Identification charts of the clusters NGC 146 (blue circle) and King 14 (red circle), based on DSS images. The circles indicate the approximate angular extent of each cluster, and the denser central regions correspond to their probable cores. The identified variable stars toward the cluster regions are marked as triangles. Bottom: Stellar surface density maps of the cluster pair, where the color scale represents the stellar density in stars per arcmin$^2$.

suggests a possible spatial proximity or partial overlap in their projected distributions. This indicates that they may share a similar location in the Galactic plane. The DSS image was obtained from the STScI Digitized Sky Survey archive.[9]

### 2.1. Gaia DR3

The Gaia mission, launched by the European Space Agency in 2013, operated until its observational phase ended in 2025. Although spacecraft operations have concluded, Gaia has continued to yield new data releases as the processing and calibration of the full mission dataset progress. Its goal is to construct a precise, extensive three-dimensional map of the the Milky Way. This map enables investigation of the intrinsic properties and kinematic behavior of its stellar populations (T. Prusti et al. 2016). The third data release of Gaia provides astrometric measurements for about 1.46 billion celestial sources (Gaia Collaboration et al. 2023; A. Vallenari et al. 2023). These include positions ($\alpha$, $\delta$), trigonometric parallaxes, and proper motions ($\mu_\alpha \cos\delta$, $\mu_\delta$). Additionally, Gaia DR3 (A. Vallenari et al. 2023) offers photometric observations in three broad passbands: the unfiltered *G* band (white light), the *BP* band (blue photometer), and the *RP* band (red photometer; T. Prusti et al. 2016; A. G. Brown et al. 2021). We applied several selection criteria to the collected data, requiring a Renormalized Unit Weight Error (RUWE) of $\leqslant$1.4 (L. Lindegren et al. 2021). In all cases, the RUWE values were $\leqslant$1.4, confirming the reliability of the Gaia astrometric solutions for the stars included in our analysis. The selected stars have trigonometric parallaxes of approximately $\varpi \approx 0.50$ mas, proper motions within $\pm$0.5 mas yr$^{-1}$, and *G*-band magnitudes of $\leqslant$20.1, based on the mean values reported in the literature.

### 2.2. ALLWISE

The Wide-field Infrared Survey Explorer data release (ALLWISE) mission provides mid-infrared photometric measurements of celestial sources in four bands, with effective wavelengths centered at 3.35 $\mu$m (W1), 4.60 $\mu$m (W2), 11.56 $\mu$m (W3), and 22.09 $\mu$m (W4; E. L. Wright et al. 2010). In the present study, we extracted photometric data from the ALLWISE source catalog for the regions surrounding the clusters NGC 146 and King 14. These mid-infrared observations are particularly valuable for probing the presence of circumstellar dust and detecting potential infrared excesses among cluster members, which may indicate ongoing or past disk activity.

### 2.3. 2Mass

This study used Two Micron All-Sky Survey (2MASS) data for these clusters. This dataset has been collected via the two highly automated 1.3 m telescopes, one at Mt. Hopkins, Arizona, USA, and the other at CTIO, Chile, with three-channel cameras (256 $\times$ 256 array of HgCdTe detectors). The 2MASS database comprises photometric data in the near-infrared *J*, *H*, and *K* bands, reaching limiting magnitudes of 15.8, 15.1, and 14.3, respectively. This data have a signal-to-noise ratio (S/N) greater than 10. We performed a cross-match of our dataset with 2MASS data using the Topcat[10] software.

### 2.4. Panstars1

The Panoramic Survey Telescope and Rapid Response System 1 (K. Hodapp et al. 2004) provides photometric data in five broadband filters: *g*, *r*, *i*, *z*, and *y*, covering a wavelength range from approximately 400 nm to 1 $\mu$m (C. W. Stubbs et al. 2010). These filters have effective wavelengths of 481, 617, 752, 866, and 962 nm, respectively (E. Schlafly et al. 2012; J. Tonry et al. 2012). The typical 5$\sigma$ limiting magnitudes for point sources in the *g*, *r*, *i*, *z*, and *y* bands are 23.3, 23.2, 23.1, 22.3, and 21.4 mag, respectively (K. C. Chambers et al. 2016).

### 2.5. TESS

The Transiting Exoplanet Survey Satellite (TESS) is equipped with four 2K $\times$ 2K charge-coupled devices (CCDs), offering a combined field of view (FOV) of 24° $\times$ 96° and an angular resolution of approximately $\sim$21″ pixel$^{-1}$ (G. R. Ricker et al. 2015). TESS observes the sky in segments called *sectors*, each spanning two orbits (27 days), with the FOV shifting by 27° along the ecliptic between sectors. It performs continuous-time-series photometry in the 600–1000 nm range (roughly equivalent to the Cousins *I*-band), suitable for detecting stellar variability. During the primary mission (Sectors 1–26), TESS provided full-frame images (FFIs) at a 30 minute cadence. In the

[9] https://stdatu.stsci.edu/

[10] https://www.star.bris.ac.uk/~mbt/topcat/

first extended mission (Sectors 27–55), the cadence improved to 10 minutes, and from Sector 56 onward, short-cadence (200 s) target pixel files (TPFs) are available for selected sources. All data products are processed using the TESS Science Processing Operations Center (SPOC) pipeline.[11] In this study, we utilized TESS photometric data from multiple sectors (17, 18, 54, 58, 78, and 85) to analyze stellar variability toward the clusters King 14 and NGC 146. All the TESS data used in this paper can be found in the Mikulski Archive for Space Telescopes (TESS Team 2021).

## 3. Kinematic Membership Analysis of Stars

NGC 146 and King 14 are young OCs situated near the Galactic plane, with Galactic latitudes of $0.^{\circ}504$ and $0.^{\circ}379$, respectively. Their positions in these low-latitude regions result in the observed stellar fields being heavily contaminated by foreground and background field stars. This contamination can significantly bias the determination of cluster parameters such as distance, reddening, age, and mass function. Therefore, obtaining a clean sample of probable cluster members is a critical step in our analysis. To determine cluster membership, we selected stars based on their locations in both the vector-point diagram (VPD) and the color–magnitude diagrams (CMDs). Probable cluster members were identified as those lying within a circular region of radius 0.5 and 0.6 mas yr$^{-1}$ for clusters NGC 146 and King 14, centered on the mean proper motion in the VPD. We initially adopted mean proper-motion values for NGC 146 and King 14 from the literature and defined circular regions of radius 0.50 and 0.66 mas yr$^{-1}$ around these values to extract preliminary candidate members. These radii reflect the observed spread in proper motions and represent the typical combination of intrinsic dispersion and Gaia DR3 uncertainties for stars in this magnitude range. Using this preliminary sample, we computed refined proper-motion centers, shown in Figure 2. Subsequently, we used them as input parameters for the maximum-likelihood membership analysis described below. Stars located outside this region were considered field contaminants. The top panels of Figure 2 display the proper-motion distribution: all stars (left), selected probable members (middle), and field stars (right). The bottom panels show the corresponding CMDs. The CMDs (middle) constructed from the selected members reveal a well-defined main sequence for both clusters. The VPDs are plotted using proper motions in R.A. ($\mu_{\alpha*} = \mu_{\alpha}\cos\delta$) and decl. ($\mu_{\delta}$).

We derived membership probabilities using the method of L. Balaguer-Núnez et al. (1998). This approach modifies and generalizes the classical maximum-likelihood method from W. Sanders (1971). The Sanders method was based on the two-component Gaussian model of S. Vasilevskis et al. (1958). This method minimizes field contamination and has been successfully applied in several recent Gaia-based studies (D. Bisht et al. 2020; D. P. Sariya et al. 2021, 2023; K. Belwal et al. 2024; N. Panwar et al. 2024; T. Chand et al. 2025). For the cluster- and field-star distributions, two distinct frequency distribution functions, $\phi_c^{\nu}$ and $\phi_f^{\nu}$, are constructed for each $i$th star. These functions are defined as follows:

$$\phi_c^{\nu} = \frac{1}{2\pi\sqrt{(\sigma_c^2+\epsilon_{xi}^2)(\sigma_c^2+\epsilon_{yi}^2)}} \times exp\left\{-\frac{1}{2}\left[\frac{(\mu_{xi}-\mu_{xc})^2}{\sigma_c^2+\epsilon_{xi}^2}+\frac{(\mu_{yi}-\mu_{yc})^2}{\sigma_c^2+\epsilon_{yi}^2}\right]\right\}$$

and

$$\phi_f^{\nu} = \frac{1}{2\pi\sqrt{(1-\gamma^2)}\sqrt{(\sigma_{xf}^2+\epsilon_{xi}^2)(\sigma_{yf}^2+\epsilon_{yi}^2)}} \times exp\left\{-\frac{1}{2(1-\gamma^2)}\left[\frac{(\mu_{xi}-\mu_{xf})^2}{\sigma_{xf}^2+\epsilon_{xi}^2}-\frac{2\gamma(\mu_{xi}-\mu_{xf})(\mu_{yi}-\mu_{yf})}{\sqrt{(\sigma_{xf}^2+\epsilon_{xi}^2)(\sigma_{yf}^2+\epsilon_{yi}^2)}}+\frac{(\mu_{yi}-\mu_{yf})^2}{\sigma_{yf}^2+\epsilon_{yi}^2}\right]\right\},$$

where ($\mu_{xi}$, $\mu_{yi}$) are the PMs of the $i$th star. PM errors are represented by ($\epsilon_{xi}$, $\epsilon_{yi}$). The PM center of the cluster is given by ($\mu_{xc}$, $\mu_{yc}$), while ($\mu_{xf}$, $\mu_{yf}$) represent the PM values of the center of the field. The intrinsic PM dispersion for cluster stars is denoted by $\sigma_c$, and $\sigma_{xf}$ and $\sigma_{yf}$ provide the intrinsic PM dispersions for the field populations. The correlation coefficient $\gamma$ is calculated as

$$\gamma = \frac{(\mu_{xi}-\mu_{xf})(\mu_{yi}-\mu_{yf})}{\sigma_{xf}\,\sigma_{yf}}.$$

Stars with proper-motion (PM) errors of $\leqslant$0.5 mas yr$^{-1}$ have been used to determine $\phi_c^{\nu}$ and $\phi_f^{\nu}$. A group of stars is found at $\mu_{xc} = -2.86$ mas yr$^{-1}$, $\mu_{yc} = -0.45$ mas yr$^{-1}$ for NGC 146, and $\mu_{xc} = -3.27$ mas yr$^{-1}$, $\mu_{yc} = -0.98$ mas yr$^{-1}$ for King 14. Assuming distances of 2.76 and 2.36 kpc from E. L. Hunt & S. Reffert (2024) for clusters and a radial velocity dispersion of 1 km s$^{-1}$ for open star clusters (T. M. Girard et al. 1989), the expected dispersion ($\sigma_c$) in PMs would be approximately 0.08 mas yr$^{-1}$ for both the clusters. Observations indicate that OCs typically exhibit internal velocity dispersions of 0.5–2 km s$^{-1}$ (A. M. Geller et al. 2010), which motivates the value adopted in this analysis. The membership probabilities remain relatively stable for velocity dispersions within this range; however, adopting higher values tends to increase the level of field-star contamination (K. Belwal et al. 2025). All cluster and field proper-motion distribution parameters were derived using the maximum-likelihood method of L. Balaguer-Núnez et al. (1998), which optimizes the two-component Gaussian model

[11] https://heasarc.gsfc.nasa.gov/docs/tess/documentation.html

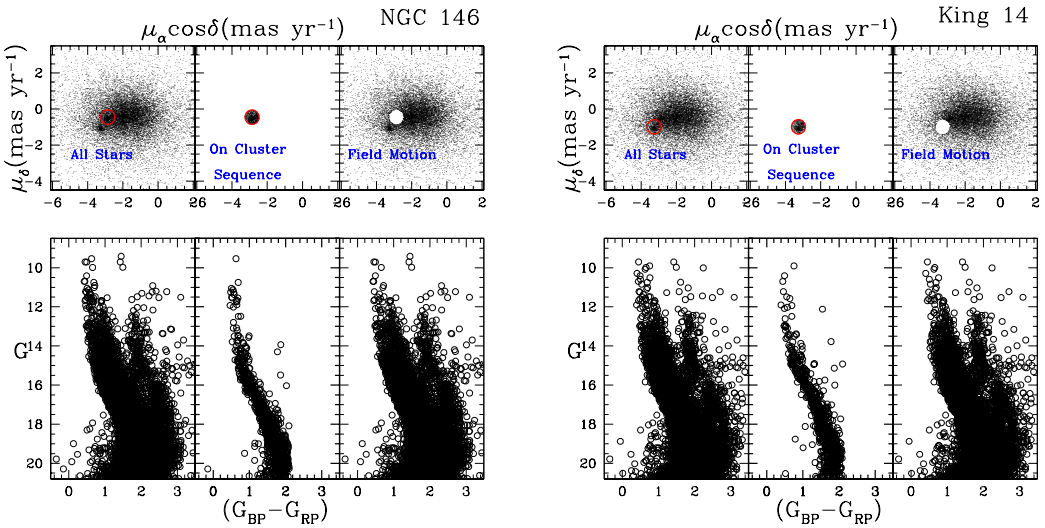


**Figure 2.** Top: Vector-point diagrams (VPDs) for NGC 146 (left group) and King 14 (right group), showing the distribution of proper motions in R.A. ($\mu_\alpha \cos\delta$) and decl. ($\mu_\delta$). For each cluster, the three panels correspond to all stars (left), stars lying on the cluster sequence (middle), and field stars (right). The red circles with radii of 0.5 and 0.6 mas yr$^{-1}$ for NGC 146 and King 14, respectively, indicate the proper-motion selection used to define probable cluster members. Bottom: Corresponding Gaia DR3 color–magnitude diagrams, $G$ versus ($G_{BP} - G_{RP}$), for the same samples (all stars, probable members, and field stars) in the direction of NGC 146 (left) and King 14 (right).

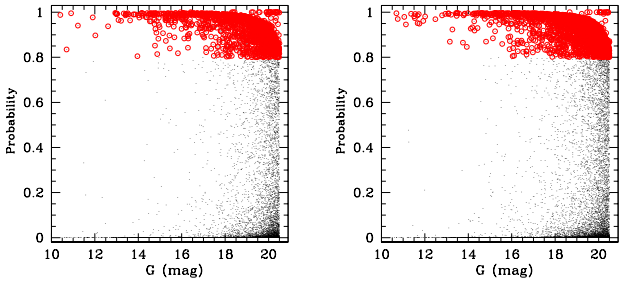


**Figure 3.** Membership probability as a function of Gaia $G$-band magnitude for stars in the regions of NGC 146 (left) and King 14 (right), derived using the method of L. Balaguer-Núnez et al. (1998). Red circles indicate stars with membership probability greater than 80%, considered as probable cluster members.

to the Gaia DR3 data. For field-region stars, we have estimated ($\mu_{xf}$, $\mu_{yf}$) = (−1.8, 0.4) mas yr$^{-1}$ for NGC 146 and ($\mu_{xf}$, $\mu_{yf}$) = (−3.2, −1.8) mas yr$^{-1}$ for King 14, with ($\sigma_{xf}$, $\sigma_{yf}$) = (3.5, 3.9) and (4.2, 3.4) mas yr$^{-1}$ for both the clusters, respectively.

Considering the normalized numbers of cluster stars and field stars as $n_c$ and $n_f$ respectively (i.e., $n_c + n_f = 1$), the total distribution function can be calculated as

$$\phi = (n_c \times \phi_c^{\nu}) + (n_f \times \phi_f^{\nu}).$$

As a result, the membership probability for the $i$th star is given by

$$P_\mu(i) = \frac{\phi_c(i)}{\phi(i)}.$$

Using this method, we identified 770 and 690 stars as cluster members for NGC 146 and King 14, respectively, with membership probabilities higher than 80% and $G \leqslant 20$ mag. In Figure 3, we plot the likelihood of membership versus magnitude $G$ for both clusters. The T. Cantat-Gaudin et al. (2018) catalog provides membership probabilities for all clusters studied. We matched our likely members with this catalog and identified 138 stars for NGC 146 and 153 stars for King 14, which are common. In the CMDs, blue dots represent the matched stars, while black dots indicate those with membership probabilities higher than 80%. We adopted a membership probability threshold of 80% to minimize contamination, in particular at the fainter end of the cluster sequence. Several threshold values were tested, and we found that adopting lower probabilities led to increased contamination from field stars in the faint region of the CMD. Thus, a threshold of 80% was adopted to achieve an optimal compromise between member-star and field-star contamination. The mean proper motions derived for these clusters are ($\mu_\alpha \cos\delta$, $\mu_\delta$) = (−2.81 ± 0.14, −0.47 ± 0.21) mas yr$^{-1}$ for NGC 146 and (−3.23 ± 0.18, −0.97 ± 0.21) mas yr$^{-1}$ for King 14. These values are in good agreement with the measurements reported by W. S. Dias et al. (2021), validating our membership determination and supporting the kinematic coherence of the NGC 146–King 14 pair.

The close agreement in proper motions, parallaxes, and spatial positions of both clusters provides strong evidence for a common bulk motion through the Galaxy. Their kinematic coherence, along with similar ages and distances, strongly indicates a comoving origin. These results suggest that both clusters may represent a physically associated pair formed within the same giant molecular cloud complex. The detailed assessment of their relative separation, orbital parameters, and dynamical binding is discussed in the following sections, to examine whether they constitute a primordial binary cluster system or a dynamically unbound comoving pair within the Galactic disk.

## 4. Physical Characterization of OCs

### 4.1. Radial Density Profile

The center coordinates of each cluster, NGC 146 (R.A. = 8.262, decl. = 63.293) degrees and King 14 (R.A. = 7.965, decl. = 63.162) degrees, were determined as the positions corresponding to the maximum stellar surface density. These locations were identified from a two-dimensional stellar density map, constructed by performing uniform binning in R.A. and decl. The derived central coordinates are in good agreement with those reported by W. S. Dias et al. (2021) and

**Table 1**
Structural Parameters of the Clusters under Study

| Parameter | NGC 146 | King 14 |
|---|---|---|
| $f_0$ (stars/arcmin$^2$) | 19.28 | 12.17 |
| $f_b$ (stars/arcmin$^2$) | 6.20 | 3.20 |
| $r_c$ (arcmin) | 0.93 | 2.20 |
| $r_c$ (pc) | 0.66 | 1.70 |
| $r_t$ (pc) | 11.0 | 14.0 |
| $\delta_c$ | 4.1 | 4.8 |
| $r_{\rm lim}$ (arcmin) | 7.0 | 10.5 |
| $c$ | 0.58 | 0.47 |

**Notes.** Background and central densities are in units of stars per arcmin$^2$. Core radius ($r_c$) and limiting radius ($r_{\rm lim}$) are given in arcminutes and parsecs. $r_t$ is tidal radius in pc.

are consistent with the positional uncertainties provided in the catalog of T. Cantat-Gaudin et al. (2018).

To analyze the stellar distribution, we constructed radial density profiles (RDPs) for NGC 146 and King 14 by dividing the cluster region into concentric annular rings of width 1.′0, centered on the estimated cluster centers. The stellar surface density in the $i$th ring, $\rho_i$, was calculated using the standard relation:

$$\rho_i = \frac{N_i}{A_i},$$

where $N_i$ is the number of stars within the $i$th annulus, and $A_i = \pi(r_{i+1}^2 - r_i^2)$ is its area.

To further characterize the structural properties of the clusters, we fitted the observed RDPs using the modified empirical King profile (I. King 1962):

$$f(r) = f_0 \left[ \frac{1}{\sqrt{1 + (r/r_c)^2}} - \frac{1}{\sqrt{1 + (r_t/r_c)^2}} \right]^2 + f_b, \quad (1)$$

where $f(r)$ is the stellar surface density at radius $r$, $f_0$ is the central density above the background level, $f_b$ is the background field-star density, $r_c$ is the core radius, and $r_t$ is the tidal radius of the cluster. All estimated structural parameters are listed in Table 1. The radius of the cluster was chosen as the radial distance at which the stellar surface density flattens and merges with the background field-star density. Based on this criterion, we found $r_{\rm lim} \sim 7.'0$ for NGC 146 and $r_{\rm lim} \sim 10.'5$ for King 14, as shown in Figure 4. Beyond these radii, the stellar density remains nearly constant, demonstrating the change from cluster- to field-dominated regions. In addition to the cluster radius, this model provided a good fit to the observed profiles, yielding estimates of the core radius, tidal radius, and central density that offer insights into the dynamical state and spatial extent of the clusters under study.

According to G. Maciejewski & A. Niedzielski (2007), the limiting radius ($r_{\rm lim}$) of an open cluster typically lies in the range of approximately $2r_c$ to $7r_c$, depending on the dynamical state and external tidal effects acting on the cluster. For NGC 146 and King 14, our derived values of $r_{\rm lim}$ and $r_c$ yield $r_{\rm lim}/r_c$ ratios of ∼7.53 and ∼4.78, respectively, which fall well within this expected range. This consistency indicates that the structural parameters obtained from our King model fit well with the general properties of OCs as reported in the literature.

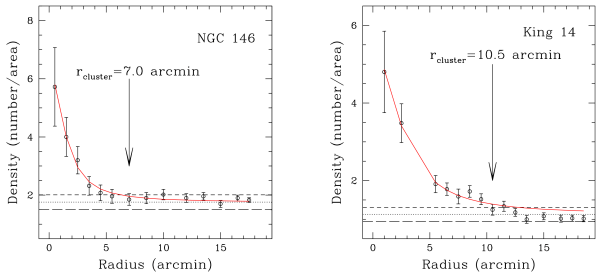


**Figure 4.** RDPs of NGC 146 (left) and King 14 (right), constructed using the surface stellar density in concentric annuli centered on each cluster. The observed data points (black dots) represent the stellar density, with vertical error bars indicating Poisson uncertainties. The solid red curves show the best-fit I. King (1962) model profiles. The horizontal dashed lines represent the estimated background field-star density, while the arrows mark the adopted cluster radii ($r_{\rm cluster}$) of 7.′0 for NGC 146 and 10.′5 for King 14. These fits enable the determination of structural parameters such as core radius, background density, and limiting radius.

To further assess the structural concentration of the clusters, we computed the density-contrast parameter $\delta_c$, defined as

$$\delta_c = 1 + \frac{f_0}{f_b}.$$

The parameter $\delta_c$ provides a measure of how prominently the cluster stands out against the field. The resulting $\delta_c$ values are found to be ∼4.1 for NGC 146 and ∼4.8 for King 14. These values are somewhat lower than the contrast range ($7 \leqslant \delta_c \leqslant 23$) reported for compact, rich clusters by C. Bonatto & E. Bica (2007), suggesting that both clusters are relatively loose or moderately concentrated. Such low contrast values are typical of young or dynamically evolving clusters in dense Galactic fields.

The derived structural parameters provide valuable insights into the internal morphology and dynamical state of the clusters. NGC 146 has a relatively small core radius ($r_c = 0.66$ pc), with most stars concentrated toward the center, indicating a higher degree of central concentration than King 14. King 14 exhibits a larger core radius ($r_c = 1.70$ pc) compared to NGC 146. This difference may indicate a more dynamically evolved structure, but it may also arise from differences in the initial size of the parent molecular cloud. A larger core radius alone does not demonstrate physical expansion. Detecting true dynamical expansion would require observing systematic radial gradients in the internal proper-motion field; however, the Gaia DR3 proper-motion uncertainties at the distance of these clusters are too large to reveal such subtle signatures. Thus, while we cannot assert greater dynamical evolution with certainty, the larger core radius provides a strong indication consistent with that scenario. Both clusters exhibit modest density-contrast parameters ($\delta_c \sim 4$–5), typical of young OCs in dense Galactic environments, where tidal interactions and external perturbations play significant roles in shaping their evolution. The RDPs of both clusters display extended outer regions and gradual declines in stellar density, suggesting possible tidal distortion or halo overlap due to interactions with the Galactic gravitational field or with each other. Based on the King model fits, the estimated tidal radii are ∼11 pc for NGC 146 and ∼14 pc for King 14, indicating that both clusters are well-confined within their tidal boundaries. The larger tidal radius of King 14, consistent with its older age and higher mass, implies it has undergone a longer period of dynamical evolution under Galactic tidal

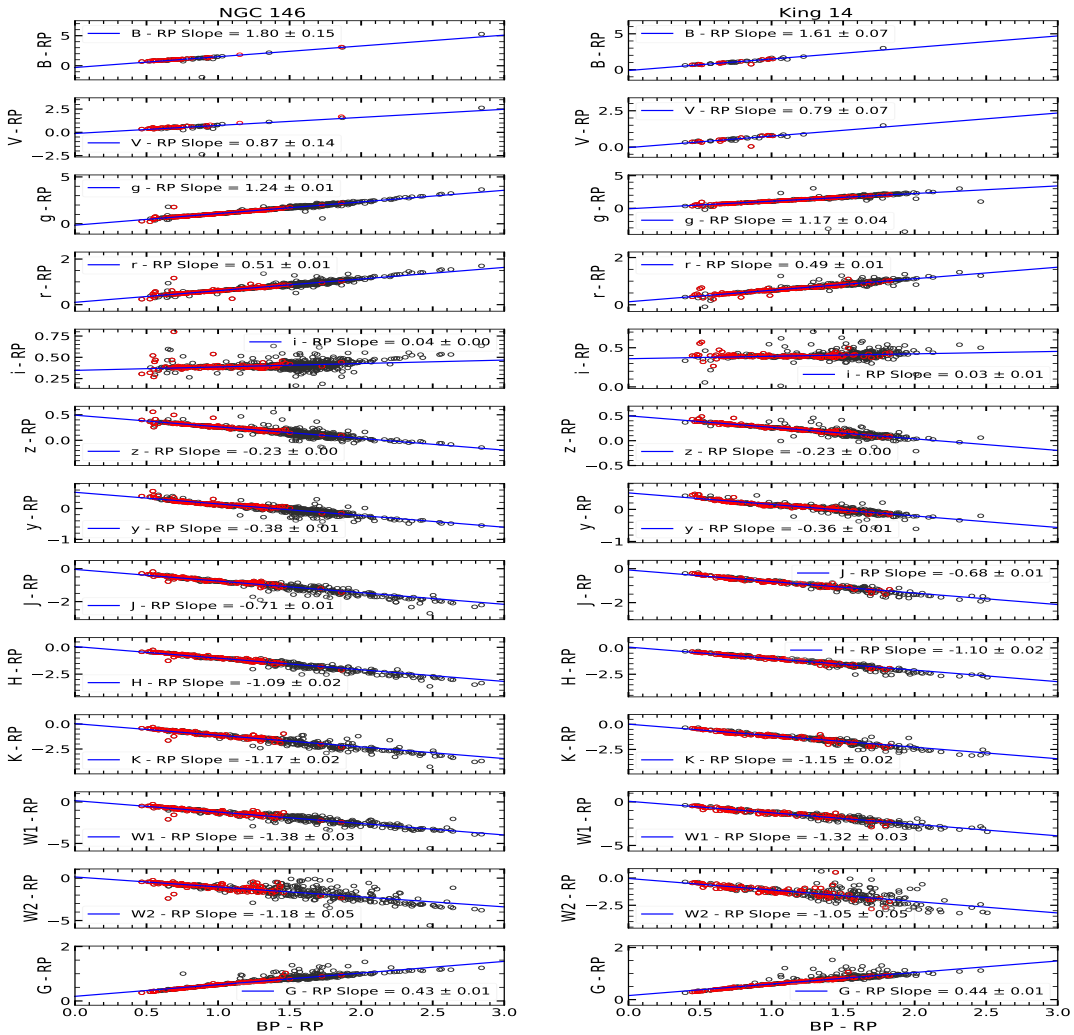


**Figure 5.** Two-color diagrams (TCDs) for the clusters NGC 146 (left panels) and King 14 (right panels), constructed using combinations of optical to near-infrared photometric bands (e.g., *B*, *V*, *g*, *r*, *i*, *z*, *y*, *J*, *H*, *K*, W1, W2, *G*) against Gaia $G_{RP}$ magnitudes. The diagrams illustrate the photometric transformations and interband correlations, with linear fits overplotted in each panel. These TCDs are employed to probe the interstellar extinction law across different wavelengths and help in constraining the total-to-selective extinction ratio ($R_V$), offering insights into the dust properties along the line of sight toward the clusters.

**Table 2**
Derived Color-excess Ratios $(\lambda - G_{RP})/(G_{BP} - G_{RP})$ for Various Photometric Filters along the Line of Sight toward the OCs NGC 146 and King 14

| Filter ($\lambda$) | Wavelength (nm) | $\frac{\lambda - G_{RP}}{G_{BP} - G_{RP}}$ | |
|---|---|---|---|
| | | NGC 146 | King 14 |
| Johnson B | 445 | 1.796 ± 0.154 | 1.610 ± 0.068 |
| Johnson V | 551 | 0.867 ± 0.144 | 0.795 ± 0.067 |
| Pan-STARRS g | 481 | 1.243 ± 0.009 | 1.170 ± 0.041 |
| Pan-STARRS r | 617 | 0.511 ± 0.006 | 0.490 ± 0.007 |
| Pan-STARRS i | 752 | 0.045 ± 0.004 | 0.035 ± 0.005 |
| Pan-STARRS z | 866 | −0.228 ± 0.004 | −0.235 ± 0.004 |
| Pan-STARRS y | 962 | −0.378 ± 0.006 | −0.360 ± 0.006 |
| 2MASS J | 1234.5 | −0.708 ± 0.013 | −0.679 ± 0.017 |
| 2MASS H | 1639.3 | −1.085 ± 0.016 | −1.095 ± 0.018 |
| 2MASS K | 2175.7 | −1.167 ± 0.022 | −1.149 ± 0.025 |
| ALLWISE W1 | 3317.2 | −1.378 ± 0.025 | −1.322 ± 0.025 |
| ALLWISE W2 | 4550.1 | −1.176 ± 0.046 | −1.053 ± 0.054 |
| Gaia *G* | 641.9 | 0.428 ± 0.006 | 0.443 ± 0.009 |

**Note.** These ratios were obtained using multiwavelength photometric data from Johnson, Pan-STARRS, 2MASS, ALLWISE, and Gaia passbands to characterize the wavelength dependence of interstellar reddening in the direction of the clusters.

influence. The $r_t/r_c$ ratios of ∼17 and ∼8 for NGC 146 and King 14, respectively, are typical of moderately concentrated young clusters. The comparable structural morphology and overlapping spatial extents of the two systems support the view that NGC 146 and King 14 likely originated within the same molecular complex and are presently evolving as a comoving, dynamically unbound pair within the Galactic disk.

### 4.2. Extinction Law from Optical to Mid-infrared Photometry

In this section, we use all the datasets to examine the extinction law from the optical to the mid-infrared region toward the clusters under study. The resulting two-color diagrams (TCDs), plotted as $(\lambda - G_{RP})/(G_{BP} - G_{RP})$, are presented in Figure 5 for all clusters. Here, $\lambda$ represents the filters other than $G_{RP}$. All stars shown in Figure 5 plotted in black represent the probable cluster members, while the red open circles indicate the matched stars from T. Cantat-Gaudin et al. (2018). A linear fit was applied to the data points, and the resulting slopes are listed in Table 2. The estimated slope values are in good agreement with those reported by S. Wang & X. Chen (2019) and D. Bisht et al. (2020). We calculated the ratio $\frac{A_V}{E(B-V)}$ as 3.02 for NGC 146 and 3.03 for King 14. These

values are very close to the standard value of 3.1, indicating that the reddening law toward the regions of both clusters is consistent with the normal interstellar extinction law. The close agreement in the extinction law and reddening values shows that both clusters are affected by a similar interstellar medium. This similarity suggests that they are at comparable distances along the same line of sight and likely share the same intervening dust layer. The following sections examine their spatial separation and kinematics for further insight into their possible association.

## 5. Fundamental Parameter Estimation of the Cluster Pair

### 5.1. Distance of Clusters from Trigonometric Parallax

To calculate the distance between the clusters under study, we first selected the most probable members with a probability greater than 80%. Next, we fitted a Gaussian curve to the parallax histogram to determine the mean trigonometric parallax, excluding stars with negative parallax. We obtained mean parallax values of 0.320 mas for NGC 146 and 0.380 mas for King 14. Following this, we applied a zero-point offset of −0.021 mas to the mean trigonometric parallax, as recommended by M. Groenewegen (2021). We estimated the cluster distances by directly inverting the trigonometric parallaxes, which may be inaccurate. This approach yields values of $3.125 \pm 0.450$ kpc for NGC 146 and $2.632 \pm 0.310$ kpc for King 14, respectively. We followed the method of C. A. Bailer-Jones (2015), which shows that a probabilistic approach yields more precise estimates, in particular when accounting for trigonometric parallax errors. Building on this insight, they proposed a Bayesian approach that incorporates both the measured trigonometric parallax and its uncertainty. We therefore adopted the methodology from C. Bailer-Jones et al. (2018) to measure the distance. A comprehensive description of the methods we used is provided in K. Belwal et al. (2025). Consequently, the estimated distances, $2.98 \pm 0.33$ kpc and $2.51 \pm 0.23$ kpc, are in good agreement with those reported by T. Cantat-Gaudin et al. (2018) and E. L. Hunt & S. Reffert (2024). We used these distance values for further analysis of the cluster.

Determining the age and distance of clusters is vital to understanding their evolution, dynamics, and role in the Milky Way's structure. In this study, we utilized multiband photometric data from Gaia, WISE, and Pan-STARRS to construct precise color–magnitude diagrams (CMDs) for NGC 146 and King 14. We include the near-infrared ($J$, $J-H$) CMD to provide an independent consistency check using 2MASS photometry. However, the isochrones reproduce only the bright part of the NIR main sequence. For $J \geqslant$ 13–14 mag, 2MASS photometry becomes increasingly incomplete, and photometric uncertainties multiply, leading to a broadened, poorly defined lower main sequence. In addition, for young clusters (20–50 Myr), the low-mass main sequence is nearly vertical in ($J-H$), limiting the diagnostic power of faint NIR data. Therefore, we primarily rely on Gaia CMDs to determine the cluster parameters, and use the 2MASS CMD only as a complementary check at the bright end. To minimize field-star contamination and ensure reliable cluster membership, we applied selection criteria based on proper motion and trigonometric parallax. This astrometric filtering allowed us to identify probable members with high confidence. We performed isochrone fitting using PARSEC models by P. Marigo et al. (2017) at solar metallicity ($Z = 0.02$), employing photometric sets: ($G$, $G_{\rm BP} - G_{\rm RP}$) from Gaia, ($J$, $J - H$) from 2MASS, and ($g$, $g - i$) from Pan-STARRS. Since the color-excess ratios (Table 2) indicate that the clusters follow a normal extinction law ($R_{\rm v} \approx 3.1$), we adopt standard extinction coefficients for all passbands and derive the absolute reddening directly from CMD isochrone fitting. Parameters from isochrone fitting for each cluster are detailed below.

#### NGC 146

The CMDs for NGC 146 (see Figure 6) exhibit a well-defined and tight main sequence extending down to fainter magnitudes, indicative of a relatively young stellar population. Isochrone fitting was performed for log(age) values between 7.2 and 7.4. The best global fit was achieved for log(age) = 7.3, corresponding to an age of 20 ± 5 Myr. The cluster parameters were estimated via isochrone fitting using the chi-square minimization technique, yielding a reduced chi-square value of 0.85. The apparent distance modulus was estimated to be $(m - M) = 13.90 \pm 0.24$ mag, yielding a heliocentric distance of $2.87 \pm 0.46$ kpc. This distance is consistent with the value reported by T. Cantat-Gaudin et al. (2018) and agrees well with the parallax-based distance listed in Table 3. The young age and compact structure of NGC 146 suggest that the cluster is dynamically young and possibly still undergoing early evolutionary processes.

#### King 14

King 14 exhibits a relatively more dispersed main sequence in the CMD (see Figure 6), indicative of a slightly older age and possibly some degree of dynamical evolution. For this cluster, isochrones with log(age) between 7.6 and 7.8 were overlaid, and the best fit was found at log(age) = 7.7, corresponding to an age of 50 ± 10 Myr. The cluster parameters were estimated via isochrone fitting using the chi-square minimization technique, yielding a reduced chi-square value of 0.91. The apparent distance modulus was derived as $(m - M) = 13.50 \pm 0.20$ mag, which corresponds to a heliocentric distance of $2.47 \pm 0.34$ kpc. This value is in good agreement with the parallax and consistent with previous studies. The cluster's more evolved stellar content and wider main sequence support the age estimate.

In both NGC 146 and King 14, the CMDs reveal a relative underdensity of stars near $G \simeq$ 12–13 mag (Figure 6). Since these clusters form a physical pair likely originating from the same molecular cloud, the presence of a similar feature in both CMDs is notable. Such underdensities, or main-sequence "gaps," can arise from unresolved binaries, which shift stars upward in brightness, as well as from the brief evolutionary timescale near the main-sequence turnoff, which naturally reduces the number of stars in this region. The similarity of this feature in both clusters therefore suggests that they share comparable stellar populations, binary fractions, and initial conditions, consistent with a coeval origin. The detailed information about the main-sequence gaps in CMDs has also been reported in previous studies (E. Bohm-Vitense & R. Canterna 1974; R. Sagar & U. Joshi 1978; B. L. Rachford & R. Canterna 2000; P. Hasan 2024). Overall, the derived parameters summarized in Table 3 indicate that both clusters are relatively young OCs located at similar distances within the Perseus arm of the Milky Way. Their close spatial proximity and comparable ages suggest a possible physical connection, which will be further investigated through orbital and dynamical analyses.

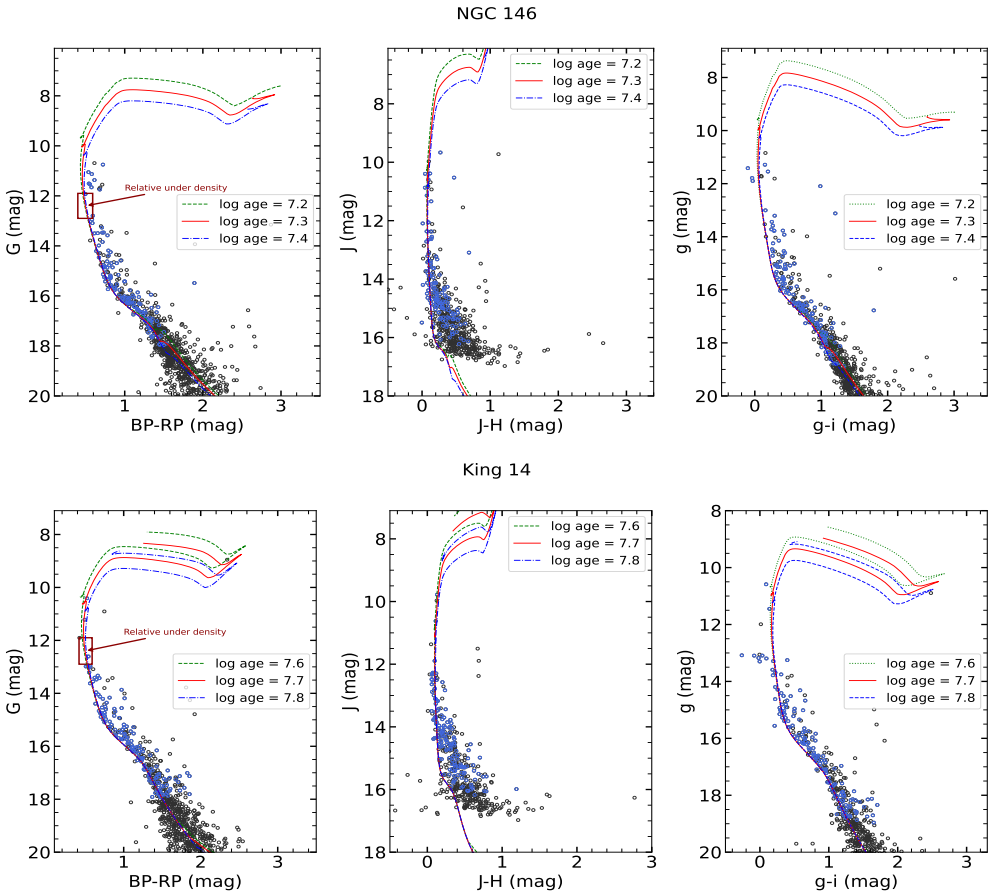


**Figure 6.** CMDs for the OCs NGC 146 (top panels) and King 14 (bottom panels) in three different photometric systems: Gaia ($G$ versus $G_{BP} - G_{RP}$), 2MASS ($J$ versus $J - H$), and Pan-STARRS ($g$ versus $g - i$). Black points represent probable cluster members identified based on our membership criteria, while blue points indicate stars that are cross-matched with the T. Cantat-Gaudin et al. (2020) catalog. Overplotted are PARSEC theoretical isochrones log(age) = 7.2, 7.3, and 7.4 for NGC 146 and 7.6, 7.7, and 7.8 for King 14, used to estimate the cluster's ages and ensure consistency across photometric bands. The alignment of cluster sequences with the isochrones across all photometric bands supports the reliability of the adopted membership selection and provides consistent age estimates for both clusters. (The data used to create this figure are available in the online article.)

For the radial velocity estimation, we used Gaia DR3 measurements for three stars in NGC 146 and six stars in King 14. Given the small sample sizes, we adopted the weighted mean method, which accounts for the individual uncertainties of each measurement. For NGC 146, this yields a mean radial velocity of $-88.457 \pm 4.613 \mathrm{km\,s^{-1}}$. Our value is consistent, within uncertainties, with that reported by E. L. Hunt & S. Reffert (2024), which was based on a single star. In the case of King 14, radial velocity values were available for six stars; however, two stars were excluded as outliers because their velocities deviated by more than $3\sigma$ from the mean of the sample. Using the remaining four stars, we obtain a mean radial velocity of $-79.075 \pm 5.348\,\mathrm{km\,s^{-1}}$.

## 6. Dynamical Study of the OCs

### 6.1. Luminosity Function and Mass Function

The luminosity function (LF) and mass function (MF) depend primarily on cluster membership and are also connected to the well-known mass–luminosity relationship. We have used $G$ versus $(G_{BP} - G_{RP})$ CMD to construct LF. We converted the $G$ magnitudes of main-sequence stars into the absolute magnitudes using the distance modulus and reddening. A histogram is constructed with 1.0 mag intervals as shown in the top panels of Figure 7. Inspection of the LF plots for both clusters reveals a steady increase in stellar density toward fainter magnitudes. There is a prominent increase in the last few bins. This behavior likely reflects the majority of low-mass stars in our sample. However, the rise could also be partially affected by residual observational biases, such as photometric incompleteness or stellar crowding at the faint end, even though our analysis is restricted to highly probable stars brighter than 20 mag and with membership probabilities above 80%.

We have used theoretical isochrones from P. Marigo et al. (2017) to convert absolute magnitudes into stellar masses, enabling a transformation of the LF into the MF. This transformation was carried out by mapping each magnitude bin to its corresponding mass bin using isochrones appropriate to each cluster's age, metallicity, and reddening. The resulting MF is expressed as the logarithm of the number of stars per unit mass interval versus the logarithm of mass, and is plotted in the lower panels of Figure 7.

The MF follows a power-law distribution of the form

$$\log\left(\frac{dN}{dM}\right) = -(1 + x)\log(M) + \text{constant}, \qquad (2)$$

where $dN$ is the number of stars in a mass bin $dM$ centered at mass $M$, and $x$ is the MF slope. A linear fit to the plotted data in logarithmic space provides the slope $x$.

**Table 3**
Comparison of the Cluster Parameters Derived in the Present Study with Those Reported in Previous Works for Clusters NGC 146 and King 14

| Author | R.A (Deg) | Decl. (Deg) | $\mu_\alpha cos(\delta)$ (mas yr$^{-1}$) | $\mu_\delta$ (mas yr$^{-1}$) | Parallax (mas) | $d_{plx}$ (kpc) | Age (Myr) | $R_{GC}$ (kpc) | $X_{GAL}$ (kpc) | $Y_{GAL}$ (kpc) | $Z_{GAL}$ (kpc) | Radial Velocity (Km s$^{-1}$) |
|---|---|---|---|---|---|---|---|---|---|---|---|---|
| | | | | | NGC 146 | | | | | | | |
| Present study | $8.262 \pm 0.345$ | $63.293 \pm 0.154$ | $-2.812 \pm 0.145$ | $-0.475 \pm 0.210$ | $0.320 \pm 0.105$ | $2.98^{+0.33}_{-0.26}$ | $20 \pm 5$ | $10.059 \pm 0.186$ | $-1.529 \pm 0.169$ | $2.558 \pm 0.283$ | $0.026 \pm 0.010$ | $-88.457 \pm 4.613$ |
| N. Kharchenko et al. (2013) | 08.226 | +63.305 | −4.170 | −2.230 | ⋯ | 2.800 | 50.2 | ⋯ | ⋯ | ⋯ | ⋯ | |
| T. Cantat-Gaudin & F. Anders (2020) | 08.2624 | +63.316 | −2.864 | −0.451 | 0.307 | 3141 | 35.5 | 10.310 | −1.611 | 2.695 | 0.028 | |
| W. S. Dias et al. (2021) | 008.2590 | 63.3302 | $-2.873 \pm 0.087$ | $-0.458 \pm 0.107$ | $0.311 \pm 0.036$ | $2.685 \pm 0.146$ | $19.1 \pm 5.2$ | ⋯ | ⋯ | ⋯ | ⋯ | |
| E. L. Hunt & S. Reffert (2024) | 008.2632 | 63.3047 | −2.841 | −0.508 | 0.3342 | 2.761 | 17.5 | ⋯ | ⋯ | ⋯ | ⋯ | −99.85 |
| A. Subramaniam et al. (2005) | 8.271 | 63.301 | ⋯ | ⋯ | ⋯ | $3.470^{.335}_{-0.305}$ | 10-16 | ⋯ | ⋯ | ⋯ | ⋯ | |
| | | | | | King 14 | | | | | | | |
| Present study | $7.965 \pm 0.321$ | $63.162 \pm 0.136$ | $-3.230 \pm 0.185$ | $-0.975 \pm 0.213$ | $0.380 \pm 0.128$ | $2.51^{+0.30}_{-0.23}$ | $50 \pm 10$ | $9.725 \pm 0.146$ | $-1.282 \pm 0.118$ | $2.158 \pm 0.200$ | $0.016 \pm 0.010$ | $-79.075 \pm 5.348$ |
| N. Kharchenko et al. (2013) | 008.014 | 63.181 | −3.75 | −1.55 | ⋯ | 2.600 | 50.1 | ⋯ | ⋯ | ⋯ | ⋯ | ⋯ |
| T. Cantat-Gaudin & F. Anders (2020) | 07.987 | 63.163 | −3.267 | −0.985 | 0.402 | 2.420 | 144.6 | 9.800 | −1.236 | 2.080 | 15 | ⋯ |
| W. S. Dias et al. (2021) | 08.004 | +63.164 | $-3.268 \pm 0.158$ | $-0.995 \pm 0.165$ | $0.400 \pm 0.064$ | $2.213 \pm 0.064$ | $45.9 \pm 23.3$ | ⋯ | ⋯ | ⋯ | ⋯ | |
| E. L. Hunt & S. Reffert (2024) | 007.98607 | 63.17061 | −3.257 | −1.084 | 0.3927 | 2.358 | 48.2 | ⋯ | ⋯ | ⋯ | ⋯ | ⋯ |
| M. Netopil et al. (2006) | 8.013 | 63.156 | ⋯ | ⋯ | ⋯ | $2.96 \pm 0.42$ | 79.4 | 10.330 | ⋯ | ⋯ | 0.020 | |

**Note.** The listed parameters include positional coordinates (R.A., decl.), kinematic properties (proper motions and radial velocity), parallaxes, distances, ages, and Galactic positions ($R_{GC}$, $X_{GAL}$, $Y_{GAL}$, $Z_{GAL}$).

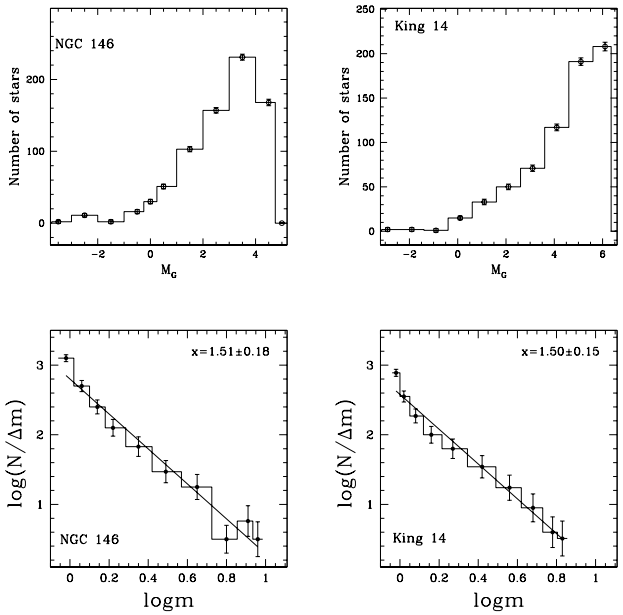


**Figure 7.** Luminosity and mass functions for the star clusters NGC 146 and King 14. The functions are plotted with fitted Salpeter power-law distributions, shown as solid lines in each panel. The derived slope (x) of the mass function is indicated within the respective panels, with uncertainties estimated using Poisson statistics ($1/\sqrt{N}$), where $N$ is the number of stars in each bin.

**Table 4**
Summary of the Derived MF Slopes and Stellar Mass Estimates for the Clusters NGC 146 and King 14

| Object | Mass Range ($M_\odot$) | MF Slope | Total Mass ($M_\odot$) | Mean Mass ($M_\odot$) |
|---|---|---|---|---|
| NGC 146 | 0.9–9.7 | 1.51 ± 0.18 | 1492 | 1.93 |
| King 14 | 0.9–6.8 | 1.50 ± 0.15 | 1250 | 1.81 |

**Note.** The table lists the stellar mass range used in the analysis, the corresponding MF slope, total cluster mass, and mean stellar mass.

For NGC 146 and King 14, the estimated MF slopes are $x = 1.51 \pm 0.18$ and $x = 1.50 \pm 0.15$, respectively. The corresponding total and mean stellar masses for both clusters are listed in Table 4. These values are slightly steeper than the canonical Salpeter (E. E. Salpeter 1955) slope of $x = 1.35$. This suggests a mild excess of low-mass stars in the observed mass range. Such slopes are typical for young OCs in the Galactic disk. They support the hypothesis of a nearly universal initial mass function (IMF), with minor deviations that may arise from local star formation conditions or early dynamical evolution. The close similarity in MF slopes between the two clusters further implies that they have experienced comparable star formation histories and subsequent dynamical evolution. Their consistent MF slopes, along with similar ages, distances, and kinematics, strengthen the argument that NGC 146 and King 14 may have originated within the same parental molecular cloud complex. A slightly steeper slope may also indicate ongoing mass segregation or the preferential loss of higher-mass members. This can occur due to internal relaxation or external tidal interactions, both of which are expected during the early stages of cluster evolution.

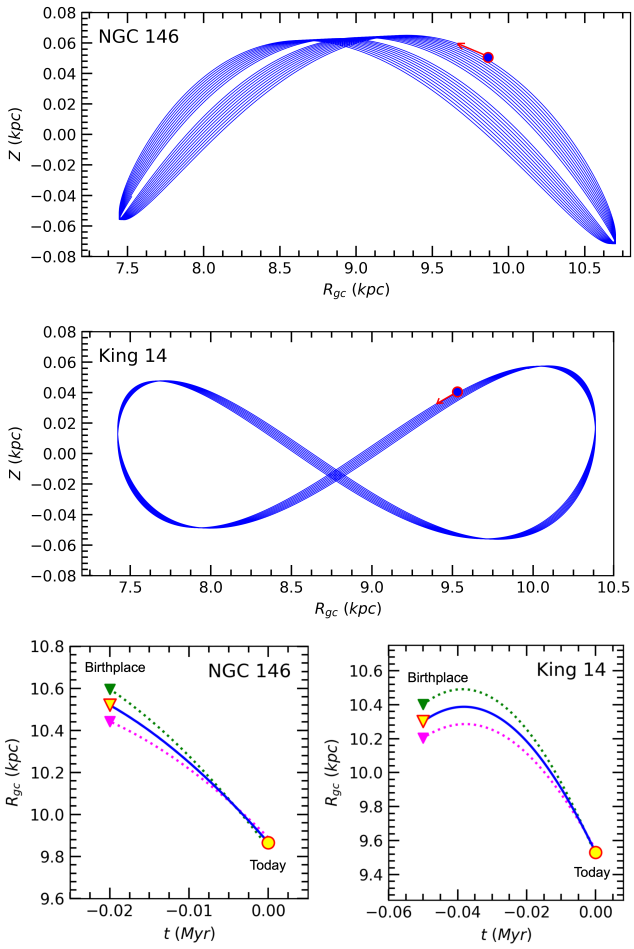


**Figure 8.** The Galactic orbits and birth radii of NGC 146 and King 14 are illustrated in two projections: $Z \times R_{gc}$ (top panels) and $R_{gc} \times t$ (bottom panels). In the bottom panel, present-day positions are indicated by filled yellow circles, while the estimated birth locations are shown as filled triangles. The dotted curves represent orbital paths computed by propagating uncertainties in the input parameters.

### 6.2. Orbital Study of OCs

We conducted a detailed dynamical analysis of NGC 146 and King 14, spatially and kinematically associated OCs, to explore their orbital properties within the Milky Way. The adopted methodology was specifically tailored for these two clusters (T. Yontan et al. 2022; D. C. Çınar et al. 2025; S. Taşdemir et al. 2025). Such studies are crucial for understanding the formation and long-term survival of binary cluster systems in the Galactic disk.

Orbital computations were performed using the axisymmetric MWPOTENTIAL2014 Galactic potential model implemented in the GALPY software package (J. Bovy 2015). This model includes critical Galactic constants, such as the Galactocentric distance of the Sun ($R_{gc} = 8.20 \pm 0.10$ kpc), the circular velocity at the solar radius ($V_{rot} = 220$ km s$^{-1}$), and the vertical displacement of the Sun from the Galactic midplane ($Z_0 = 25 \pm 5$ pc) (J. Bovy & S. Tremaine 2012). The projected Galactic orbits of NGC 146 and King 14 in different coordinate planes are shown in Figure 8.

The input parameters used in the orbit integration comprise equatorial coordinates ($\alpha$, $\delta$), heliocentric distance ($d$), mean proper-motion components ($\mu_\alpha \cos\delta$, $\mu_\delta$), and systemic radial velocities. These quantities were derived from high-precision

**Table 5**
Derived Orbital Parameters for Clusters NGC 146 and King 14

| Parameter | NGC 146 | King 14 |
|---|---|---|
| $Z_{max}$ (kpc) | 0.072 ± 0.031 | 0.058 ± 0.025 |
| $R_a$ (kpc) | 10.703 ± 0.133 | 10.387 ± 0.103 |
| $R_p$ (kpc) | 7.446 ± 0.208 | 7.422 ± 0.270 |
| $R_m$ (kpc) | 9.075 ± 0.171 | 8.905 ± 0.187 |
| $e$ | 0.179 ± 0.020 | 0.167 ± 0.023 |
| $P_{orb}$ (Myr) | 258 ± 1 | 253 ± 2 |
| $R_{teo}$ (kpc) | 10.52 ± 0.15 | 10.30 ± 0.19 |

**Note.** The listed quantities include the maximum distance from the Galactic plane ($Z_{max}$), apogalactic distance ($R_a$), perigalactic distance ($R_p$), mean orbital radius ($R_m$), orbital eccentricity ($e$), orbital period ($P_{orb}$), and present Galactocentric distance ($R_{teo}$).

astrometric and spectroscopic measurements compiled in Table 3. With these six-dimensional phase-space coordinates, we integrated the orbits of both clusters forward in time over intervals consistent with their estimated ages, using a 1 Myr time step (Z. F. Bostancı et al. 2015; W. H. Elsanhoury et al. 2025).

From the resulting orbital trajectories, we derived the apogalactic distance ($R_a$), perigalactic distance ($R_p$), mean orbital radius ($R_m = (R_a + R_p)/2$), orbital eccentricity ($e$), maximum vertical excursion from the Galactic plane ($Z_{max}$), and orbital period ($P_{orb}$). These results are listed in Table 5.

NGC 146 follows a nearly circular Galactic orbit with an eccentricity of ($e = 0.179 \pm 0.020$), oscillating between $R_p = 7.446 \pm 0.208$ kpc and $R_a = 10.703 \pm 0.133$ kpc. Its mean Galactocentric radius is $R_m = 9.075 \pm 0.171$ kpc, and the cluster reaches a maximum vertical height of only $Z_{max} = 0.072 \pm 0.031$ kpc above the Galactic plane. The orbital period of NGC 146 is calculated as 258 ± 1 Myr. King 14 exhibits similarly low orbital eccentricity ($e = 0.167 \pm 0.023$), with radial excursions ranging from $R_p = 7.422 \pm 0.270$ kpc to $R_a = 10.387 \pm 0.103$ kpc. Its mean orbital radius is $R_m = 8.905 \pm 0.187$ kpc, and its maximum vertical amplitude is $Z_{max} = 0.058 \pm 0.025$ kpc. The orbital period is computed as 253 ± 2 Myr.

The very small $Z_{max}$ values for both systems indicate that their orbits remain tightly confined to the Galactic midplane, consistent with expectations for young thin-disk clusters. Their nearly circular orbits and comparable orbital periods suggest they have experienced similar dynamical conditions throughout their lifetimes. Using the traceback early orbital radius method ($R_{teo}$), the inferred formation radii are now very close: NGC 146 at $R_{teo} = 10.53 \pm 0.15$ kpc and King 14 at $R_{teo} = 10.30 \pm 0.19$ kpc, implying that both clusters likely formed at similar Galactocentric distances.

Figure 9 shows the positions of NGC 146 and King 14 in both the Galactic $x$–$y$ plane and in three-dimensional space. Both clusters move in disk-like, low-eccentricity orbits with small vertical excursions, staying close to the Galactic plane. Their current velocities and orbital paths are similar, but they are not gravitationally bound. Table 5 confirms this: the clusters have similar orbital radii and periods, but their separation is too large for them to form a bound system. Overall, NGC 146 and King 14 form a comoving pair that travels together through the Galactic disk without being gravitationally connected.

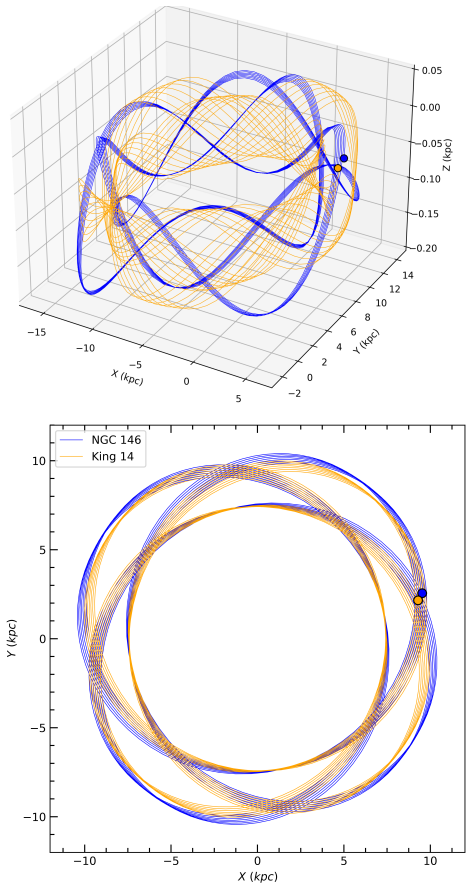


**Figure 9.** The orbits of NGC 146 and King 14 in the Milky Way. The top panel shows a three-dimensional representation of the orbits of NGC 146 (blue) and King 14 (orange), while the bottom panel displays the same orbits projected onto the $XY$ plane.

## 7. Dynamical Relationship of the NGC 146-King 14 Cluster Pair

In this study, we investigate the possible physical association between the young OCs NGC 146 and King 14, which are located in close angular proximity on the sky. The fundamental parameters derived in this work indicate that both clusters are broadly consistent with having formed in the same Galactic environment. NGC 146 and King 14 exhibit comparable ages, $\log(t) \approx 7.3$ and $\log(t) \approx 7.7$, and lie at similar heliocentric distances of 2.98 ± 0.33 kpc and 2.51 ± 0.23 kpc, respectively. Their mean proper motions derived from Gaia DR3, ($\mu_\alpha \cos\delta$, $\mu_\delta$), are also very close, indicating minimal relative tangential motion within the measurement uncertainties. The similarity in age, distance, and motion suggests a likely common origin, possibly from the same parental molecular cloud complex.

To assess their spatial association, we estimated the three-dimensional separation between the two clusters using the method of A. Subramaniam et al. (1995), which employs the clusters' equatorial coordinates and distances. This yields a positional separation of 8.97 pc, consistent with the previously reported value of 8.64 pc. Such a slight separation places the pair among close cluster pairs ($R < 20$ pc), which are typically considered candidate binaries or primordial clusters. Building on this two-dimensional analysis, we next explored their actual three-dimensional separation.

Adopting cluster masses of $M_1 = 1492\,M_\odot$ for NGC 146 and $M_2 = 1250\,M_\odot$ for King 14, the total mass of the system is $M_{\rm tot} = 2742\,M_\odot$, giving $\sqrt{M_{\rm tot}} \approx 52.4$. Using our updated orbital solutions obtained with `galpy`, the clusters exhibit similar orbital periods and eccentricities, with ($P_{\rm orb}$, $e$) = (258 Myr, 0.18) for NGC 146 and (253 Myr, 0.17) for King 14. We have used the relationship given by R. de La Fuente Marcos & C. de La Fuente Marcos (2010) to calculate the separation between these two clusters:

$$P_{\rm orb} \quad ({\rm Myr}) = 94\left(\frac{S_0}{1+e_0}\right)^{3/2}\frac{1}{\sqrt{M_1+M_2}}, \tag{3}$$

where $P_{\rm orb}$ is the orbital period, $S_0$ is the present-day three-dimensional separation between the clusters, $e_0$ is the orbital eccentricity of the pair, and $M_1$ and $M_2$ are their total masses. We have estimated $S_0 \approx 32.3$ pc for NGC 146 and $S_0 \approx 31.7$ pc for King 14. The close consistency of these values supports a characteristic dynamical separation of $S_0 \approx 32$ pc for the pair. This quantity represents the effective orbital semimajor axis the clusters would possess if they formed a gravitationally bound binary system, and should not be interpreted as the present-day geometric distance. Instead, it is a theoretical separation scale derived from their total mass, orbital period, and orbital eccentricity, corresponding to the radius required to maintain a bound configuration. Although this relatively small separation indicates a spatially coherent system, dynamical considerations show that the clusters are not gravitationally bound.

The escape velocity for a binary cluster system is given by (J. Binney & S. Tremaine 2008)

$$v_{\rm esc} = \sqrt{\frac{2GM_{\rm tot}}{R}}, \tag{4}$$

where $G = 4.302 \times 10^{-3}$ pc (km s$^{-1}$)$^2$ $M_\odot^{-1}$. At a separation of ~33 pc, the escape speed is $v_{\rm esc} \simeq 1$ km s$^{-1}$. Since the relative velocity between the clusters is on the order of a few km s$^{-1}$, the system is dynamically unbound.

The Galactic orbital analysis shows that both clusters follow nearly circular, thin-disk orbits with similar guiding radii and orbital periods of ~250–260 Myr. Their low eccentricities, comparable orbital parameters, and similarity in age, proper motion, and distance indicate that NGC 146 and King 14 are a comoving pair that likely originated in the same giant molecular cloud. At present, however, the low escape velocity and nonzero relative motion demonstrate that the pair is dispersing rather than gravitationally bound. The NGC 146–King 14 system thus represents a comoving, coborn but dynamically unbound cluster pair, providing a valuable case study for the formation and subsequent dissolution of primordial binary clusters in the Galactic disk.

## 8. Characterization of Variable Stars in the Vicinity of NGC 146 and King 14

Variable stars are powerful tracers of stellar content and the dynamical evolution of star clusters. Their pulsation or eclipsing behavior provides strong constraints on fundamental parameters. These include mass, luminosity, radius, and evolutionary state. This information allows precise calibration of cluster distance, age, and composition. Several classes of variable stars, such as eclipsing binaries, contact systems, and massive pulsators, are strongly influenced by the cluster's internal dynamics. Processes like two-body relaxation, mass segregation, binary interactions, and tidal stripping affect their distribution, survival, and frequency within a cluster. As a result, the presence and location of variable stars clearly reveal signs of dynamical aging and cluster evolution. Identifying and characterizing variable stars gives insight into both the cluster's stellar population and the dynamical processes shaping its long-term evolution. In the NGC 146–King 14 system, identifying and cataloging variable stars helps establish a more complete picture of the stellar population along the line of sight. While only one of the detected variables appears to be a likely cluster member, the remaining field variables still provide helpful information for future time-domain studies and for distinguishing cluster-associated variability from foreground or background sources. Motivated by this context, we conducted a focused variability analysis based on TESS photometry. Physical parameters were estimated only for the likely cluster-member star using spectral energy distribution (SED) fitting, which allowed us to place this object on the H–R diagram and assess its pulsational nature. The remaining variable stars are treated as field objects; their light curves are presented for completeness, but no further physical interpretation is attempted in this work, due to insufficient membership probability and limited observational coverage.

### 8.1. Derivation of Stellar Parameters from SED Fitting

To investigate the nature of the variable star TIC 444457513, identified as a likely member of the King 14 cluster, we performed a detailed SED-fitting analysis. Figure 10 presents the observed and best-fit spectral energy distribution of star TIC 444457513, along with the residuals and posterior probability distributions of the derived stellar parameters. As spectroscopic parameters such as effective temperature and luminosity are unavailable for this source, SED modeling provides a reliable means to estimate its fundamental physical properties, including effective temperature ($T_{\rm eff}$), surface gravity ($\log g$), metallicity ([Fe/H]), interstellar extinction ($A_{\rm V}$), and distance ($d$) (D. C. Çınar et al. 2024; A. Y. Alzhrani et al. 2025).

The identification of TIC 444457513 as a cluster member was based on its spatial location, photometric consistency with the cluster sequence, and distance concordance. We utilized a Bayesian SED-fitting methodology via the ARIADNE (J. I. Vines & J. S. Jenkins 2022) framework, which incorporates a diverse suite of model atmospheres and accounts for interstellar extinction. The nested sampling algorithm implemented by DYNESTY allows rigorous propagation of uncertainties in the derived parameters.

TIC 444457513 exhibits an effective temperature of $T_{\rm eff} = 11{,}826$ K and $\log g = 3.49$ cgs. Its estimated distance (2388 pc) and extinction ($A_{\rm V} = 1.22$ mag) are in excellent agreement with previous estimates for King 14, further strengthening its membership probability. The derived metallicity of [Fe/H] $= -0.21$ dex is consistent with the metal-poor nature of young open clusters located in the outer Galactic disk.

It is important to note that the metallicity inferred from SED fitting for TIC 444457513 may be affected by methodological limitations. Early-type B stars possess weak or absent metallic

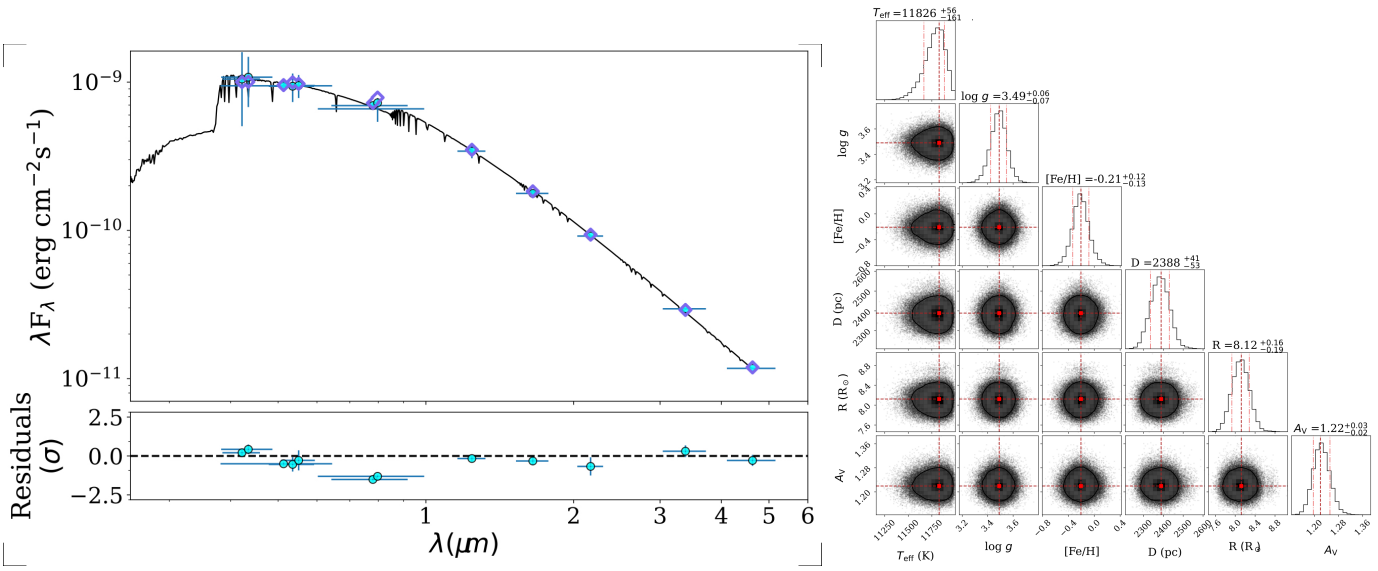


**Figure 10.** Observed and modeled spectral energy distribution (SED) of the King 14 member star TIC 444457513 (left), showing the best-fit model (solid line) and observed fluxes with uncertainties (blue points). The lower panel displays the residuals between the observed and modeled fluxes. The right panel shows the posterior probability distributions of the fitted stellar parameters from the Bayesian SED-fitting analysis.

absorption features, making accurate metallicity determination challenging. SED-based estimates for hot stars are inherently uncertain due to their smooth, continuum-dominated spectra. Additionally, photometric variability and potential circumstellar material may introduce systematic biases. Thus, the subsolar metallicity derived for TIC 444457513 may not reflect its intrinsic chemical abundance, but rather the limitations of SED fitting for hot variable stars.

Despite these caveats, SED fitting provides a robust and self-consistent framework for deriving the astrophysical parameters of TIC 444457513 in the absence of high-resolution spectroscopy. The combination of SED fitting and astrometric cross-validation allows us to characterize this variable star reliably within the King 14 cluster context.

### 8.2. H–R Diagram

We constructed a Hertzsprung–Russell (H–R) diagram using SED-derived luminosities and effective temperatures. Since most detected variable stars are field sources and not relevant to the cluster analysis, we plot only the variable star that is likely a member of King 14, TIC 444457513 (Figure 11). The star lies within the theoretical instability region of slowly pulsating B-type (SPB) stars, and we overplot the SPB instability strip and the M. J. Pecaut & E. E. Mamajek (2013) main-sequence track for reference. The remaining variable stars are not included in the diagram, as they appear to be field stars and their H–R positions do not provide additional constraints on cluster properties. Instead, we present their light curves separately without further physical interpretation. Periods were estimated using Lomb–Scargle analysis, and key variability parameters are summarized in Table 6.

### 8.3. Classification of Variable Stars

#### 8.3.1. Slowly Pulsating B-type Stars

The upper main sequence of the H–R diagram hosts SPB stars, which are main-sequence stars of spectral types B2 to B9, with effective temperatures ranging from 22,000 K to

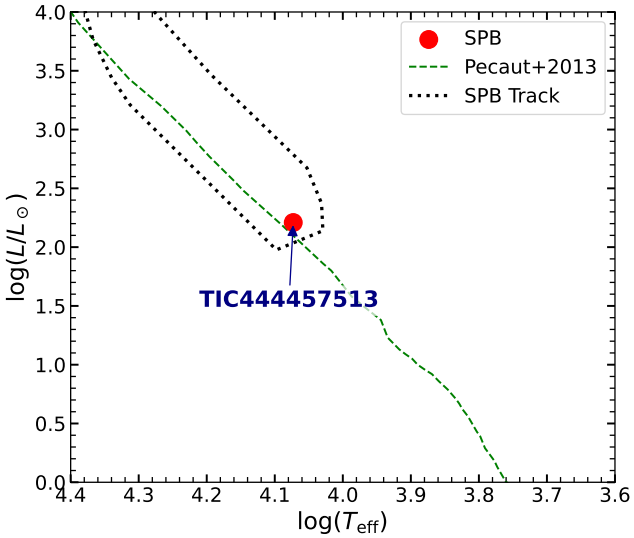


**Figure 11.** H–R diagram showing the position of selected TESS-observed star. The plot shows log($L/L_\odot$) versus log($T_{\rm eff}$), with a red circle indicating a member of the King 14 cluster. The green dashed line corresponds to a theoretical isochrone (M. J. Pecaut & E. E. Mamajek 2013), and the black dotted region marks the classical instability strip. This diagram helps to identify the evolutionary status of the observed star.

11,000 K. These stars exhibit nonradial, high-order gravity-mode ($g$-mode) oscillations that are primarily excited by the $\kappa$-mechanism at the iron opacity bump (A. Gautschy & H. Saio 1993). SPB stars typically display variability on timescales between 0.3 and 5 days (P. De Cat 2007), although more extended periods have also been observed, such as the 188 day rotational modulation of KIC 10526294 (P. Pápics et al. 2014). In the present analysis of the King 14 cluster, one SPB star was identified: TIC 444457513, exhibiting a pulsation period of 45.20 hr (1.88 days) and an effective temperature of 11,826 K. The astrometric and photometric characteristics of this object strongly support its membership in the cluster. Its position in the H–R diagram is consistent with the theoretical SPB instability strip, as illustrated in

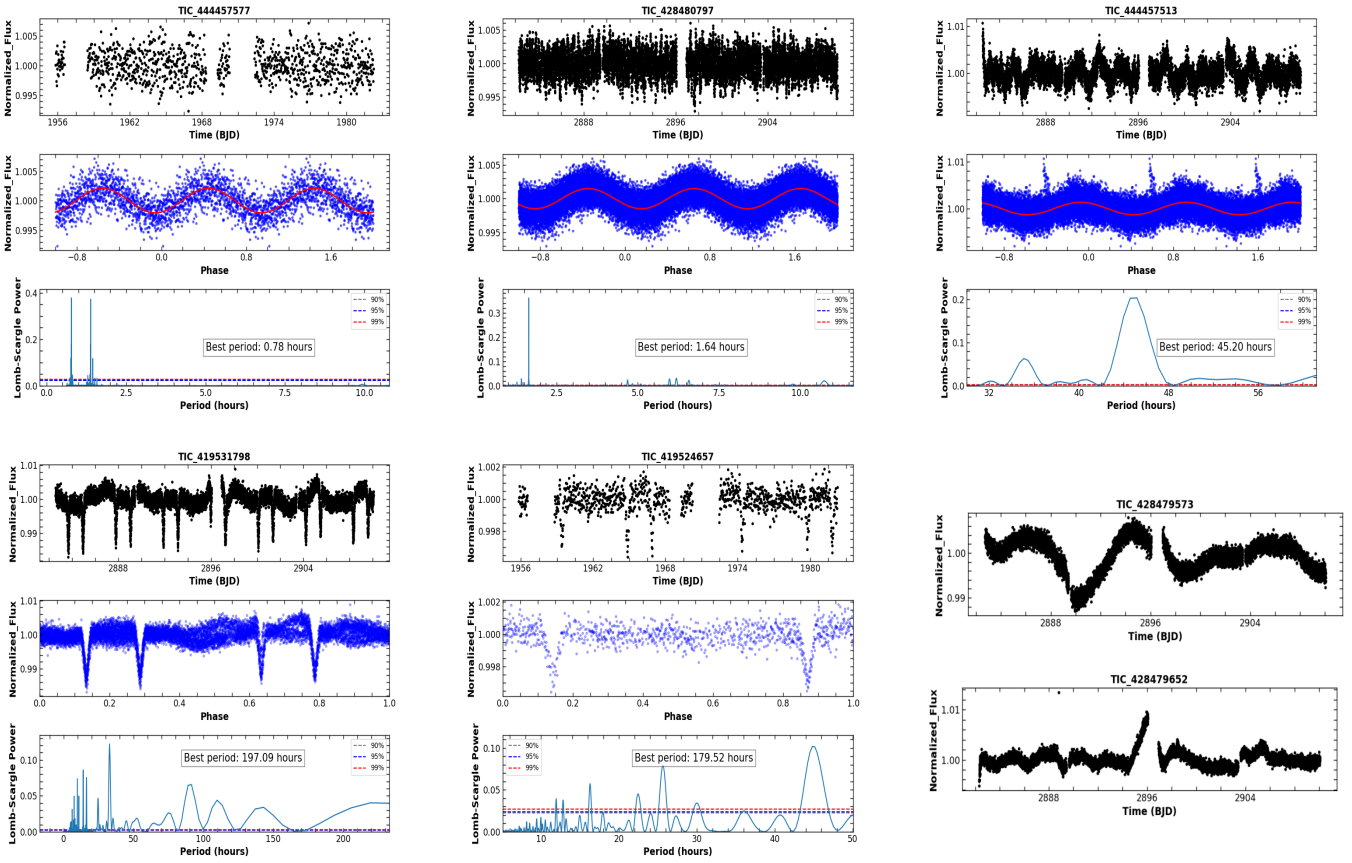


**Figure 12.** Observed light curves and periodogram analyses of selected variable stars identified in the clusters NGC 146 and King 14 using TESS data. For most stars, three vertically arranged panels are shown: the TESS light curve (top), the phase-folded light curve with the fitted model overlaid in blue (middle), and the corresponding Lomb–Scargle periodogram (bottom). For TIC 426879573 and TIC 426176052, only the TESS light curves are displayed, as reliable periodicities could not be determined, due to irregular or long-term variability.

**Table 6**
The Basic Parameters of the Variable Stars Identified in the Observed Clusters

| ID | R.A. (J2000) | Decl. (J2000) | Period (hr) | log ($T_{\rm eff}$) K | log($L/L_{\odot}$) | Membership | Type |
|---|---|---|---|---|---|---|---|
| | | | King 14 | | | | |
| TIC 444457577 | 8.09467 | 63.13414 | 0.78 | 3.8155 | 1.1139 | F | $\gamma$ Dor |
| TIC 428480797 | 7.84173 | 63.33072 | 1.64 | 3.8468 | 1.1461 | F | $\gamma$ Dor |
| TIC 444457513 | 8.08334 | 63.12024 | 45.20 | 4.0728 | 2.4329 | M | SPB |
| TIC 419531798 | 8.20497 | 63.09827 | 197.1 | 3.5548 | 2.4579 | F | EB |
| TIC 428479573 | 7.91712 | 63.02618 | ⋯ | 3.5414 | 2.7372 | F | Misc |
| TIC 428479652 | 7.71905 | 63.04594 | ⋯ | 3.5990 | 3.3234 | F | Misc |
| | | | NGC 146 | | | | |
| TIC 419524657 | 8.29757 | 63.42534 | 179.52 | 3.7865 | 1.2553 | F | Misc |

**Notes.** The columns include the TIC ID, R.A. and decl., period (in hours), effective temperature ($T_{\rm eff}$ in K), stellar luminosity, membership status, and type of variability. Membership is indicated as "*M*" for probable cluster members and "F" for field stars. The identified variability types include $\gamma$ Doradus stars, slowly pulsating B-type (SPB) stars, and an eclipsing binary. The stars are grouped by their respective clusters: NGC 146 and King 14.

Figure 11. The observed light curve and phase-folded counterpart, shown in Figure 12, clearly demonstrate periodic *g*-mode variability. The identification of a bona fide SPB star within the King 14 cluster is of considerable scientific significance. SPB stars situated in OCs benefit from accurately determined ages and metallicities, which are essential for advanced stellar modeling and asteroseismic investigations. This detection contributes to the limited catalog of confirmed SPB stars in intermediate-age clusters, deepening our understanding of pulsational phenomena in B-type stars within such environments.

### *8.4. Field and Miscellaneous Variable Stars*

Miscellaneous (Misc) variable stars exhibit variability that does not fit clearly into established classes, due to limited or inconclusive data. As these stars are not confirmed cluster members, we refrain from detailed physical interpretation.

Continued photometric monitoring may help determine their nature in future studies. The presence of Misc and field variables in the vicinity of NGC 146 and King 14 is relevant primarily from a contamination perspective. Identifying such variables helps differentiate cluster-related variability from unrelated foreground or background stars, improving membership assessments and ensuring cleaner samples for cluster-variable analyses. In this study, we identified three miscellaneous variables: TIC 428479573, TIC 428479652, and TIC 419524657. Owing to the limited number of photometric epochs (≈30), long-period behavior could not be reliably recovered, and we therefore classify all three as Misc variables without further interpretation. TIC 428479573 and TIC 428479652 have been previously flagged as long-period or semiregular variables in the literature (C. L. Watson et al. 2006; X. Chen et al. 2020), but our dataset does not provide sufficient phase coverage to confirm these periods. TIC 419524657 displays structured flux variations suggestive of eclipsing behavior; however, incomplete phase coverage prevents a conclusive classification, and it is therefore also retained in the Misc category. Although these variables are not used directly to infer cluster properties in the present study, documenting them remains valuable for future time-domain investigations. Their inclusion provides a more complete census of variability in the surrounding region, which can benefit large-scale variability surveys and help distinguish true cluster members from contaminants in subsequent membership analyses. These stars may also serve as useful comparison objects for calibration or benchmarking when more extensive photometric or spectroscopic datasets become available.

## 9. Conclusions

In this study, we have accomplished a comprehensive photometric, kinematic, and orbital investigation of the young OCs NGC 146 and King 14, aiming to understand their stellar content, dynamical state, and the nature of this comoving, dynamically unbound cluster pair. By combining multi-wavelength data from Gaia DR3, ALLWISE, Pan-STARRS1, and TESS, we have characterized cluster membership, internal structure, stellar populations, orbital dynamics, and variable star content. The main findings of this analysis are summarized below:

1. Membership analysis using the probabilistic method of L. Balaguer-Núnez et al. (1998) and Gaia DR3 astrometric data identified 770 and 690 probable members for NGC 146 and King 14, respectively, each with membership probabilities above 80%. The clear separation of clusters from field stars in the vector-point diagram supports the reliability of this selection. The resulting clean color–magnitude diagrams show defined main sequences, validating membership determination and providing a foundation for photometric and kinematic analyses.
2. Structural analysis using King profile fitting yields compact cores ($r_c = 0.66$ pc for NGC 146 and 1.70 pc for King 14) and limiting radii ($r_{lim} = 7.0'$ and $10.5'$). The derived tidal radii are $r_t = 11.0$ pc for NGC 146 and $r_t = 14.0$ pc for King 14, corresponding to tidal-to-core radius ratios of $r_t/r_c \approx 16.67$ and 8.23, respectively. These relatively moderate ratios and concentration parameters ($\delta_c \sim 4$–5) suggest that both systems are only loosely bound and dynamically evolving. Such structural characteristics, together with their young ages, are consistent with clusters undergoing early-stage mass loss and tidal interaction with the Galactic potential.
3. The clusters exhibit comparable heliocentric distances ($2.98 \pm 0.33$ kpc for NGC 146 and $2.51 \pm 0.23$ kpc), mean proper motions, and spatial locations, indicating a strong kinematic association. However, the derived orbital separation and escape velocities confirm that the pair is not gravitationally bound. Instead, NGC 146 and King 14 form a comoving, dynamically unbound cluster pair that likely originated within the same giant molecular complex in the Perseus arm.
4. Isochrone fitting shows that NGC 146 is young ($20 \pm 5$ Myr), while King 14 is slightly older ($50 \pm 10$ Myr). The modest age difference suggests formation during closely related star formation episodes within a common environment, though not from a single collapse event. Both clusters are still in early evolutionary stages, making them valuable probes for studying the transition from bound binary clusters to unbound associations.
5. The mass function slopes ($x = 1.51 \pm 0.18$ for NGC 146 and $x = 1.50 \pm 0.15$ for King 14) agree well with the classical E. E. Salpeter (1955) value, implying a normal stellar initial mass function. Evidence of mild mass segregation in both clusters indicates early internal dynamical evolution, possibly enhanced by their former proximity as a binary pair.
6. Galactic orbit integration using the `galpyMWPotential2014` model shows that both clusters follow nearly circular, low-$Z_{max}$ orbits confined to the Galactic thin disk, with orbital periods of ∼255 Myr and mean orbital radii of $R_m \sim 9$ kpc. These results indicate that NGC 146 and King 14 form a comoving but dynamically unbound pair.
7. The SED-based analysis confirms that TIC 444457513 is a probable member of King 14. Its distance modulus and line-of-sight extinction are in excellent agreement with the cluster parameters. The subsolar metallicity derived for this early-type variable ($[Fe/H] = -0.21 \pm 0.13$ dex) is lower than some literature estimates, but this likely reflects the intrinsic limitations of SED fitting for hot stars, where continuum-dominated spectra make chemical abundance determinations challenging, rather than a true deviation from the cluster composition. Overall, the stellar parameters obtained are consistent with predictions from single-star evolutionary models, demonstrating the reliability of the ARIADNE framework for characterizing stellar properties in the absence of high-resolution spectroscopy.
8. Analysis of TESS photometric time series identified several variable stars in the fields of NGC 146 and King 14, including $\gamma$ Doradus and SPB pulsators as well as eclipsing binaries. Only one of these variables appears to be a likely cluster member; the remaining sources are field stars and are not analyzed further for cluster properties. However, we provide their light curves for completeness, as cataloging variable stars in the surrounding region is valuable for future time-domain studies and for distinguishing cluster-associated variability from unrelated field sources. The confirmed

member may offer additional constraints on cluster parameters through future pulsation modeling with improved photometric coverage.

9. Altogether, the NGC 146–King 14 system provides an excellent laboratory for studying the formation and early dynamical evolution of binary OCs in the Milky Way. Their similar kinematic, structural, and orbital properties, combined with a modest age difference, strongly support a common origin within the same giant molecular cloud. However, their present-day spatial configuration and dynamical separation of $\sim$32 pc, together with relative velocities exceeding the binding threshold for their combined mass, indicate that the clusters no longer constitute a gravitationally bound binary system. Instead, they form a comoving but dynamically independent pair that is gradually dispersing under the influence of the Galactic tidal field. This system, therefore, offers a valuable test case for evaluating theoretical models of primordial cluster pairing, tidal disruption, and long-term orbital evolution in the Galactic disk. Future high-resolution spectroscopic observations and forthcoming Gaia DR4 data will be crucial for refining radial velocities, chemical abundances, and orbital constraints, allowing a more precise assessment of the clusters kinematic alignment and evolutionary link.

## Acknowledgments

We are grateful to the anonymous referee for the constructive and insightful comments that significantly improved the clarity and quality of this work. I.-G.J. acknowledges the support from the National Science and Technology Council (NSTC), Taiwan, under the grants (NSTC 113-2112-M-007-030 and NSTC 114-2112-M-007-029). We acknowledge the use of archival data from the European Space Agency's Gaia (https://www.cosmos.esa.int/gaia) mission, processed by the Gaia Data Processing and Analysis Consortium (https://www.cosmos.esa.int/web/gaia/dpac/consortium), as well as other publicly available photometric datasets from the 2MASS, Pan-STARRS1, and AllWISE. This study also utilized data from the Transiting Exoplanet Survey Satellite (TESS) mission, funded by NASA's Explorer Program. This research has used the VizieR catalog access tool, operated by the CDS, Strasbourg, France, and the NASA Astrophysics Data System (ADS). We thank the teams responsible for these surveys for making their data publicly available, which has been essential for the success of this study. D. Bisht also acknowledges the valuable discussions with collaborators and colleagues, which significantly improved the quality of this work.

*Software*: `ARIADNE` (J. I. Vines & J. S. Jenkins 2022), `galpy` (J. Bovy 2015).

## ORCID iDs

D. Bisht https://orcid.org/0000-0002-8988-8434
Ing-Guey Jiang https://orcid.org/0000-0001-7359-3300
W. H. Elsanhoury https://orcid.org/0000-0002-2298-4026
D. C. Çinar https://orcid.org/0000-0001-7940-3731
Shraddha Biswas https://orcid.org/0009-0003-8446-4557
Arvind K. Dattatrey https://orcid.org/0000-0002-4729-9316
Geeta Rangwal https://orcid.org/0000-0002-6373-770X
Devesh P. Sariya https://orcid.org/0000-0001-8452-7667

## References

Alzhrani, A. Y., Haroon, A. A., Elsanhoury, W. H., & Çınar, D. C. 2025, JApA, 46, 50
Angelo, M., Santos, J., Maia, F., & Corradi, W. 2022, MNRAS, 510, 5695
Arnold, B., Goodwin, S. P., Griffiths, D. W., & Parker, R. J. 2017, MNRAS, 471, 2498
Bailer-Jones, C., Rybizki, J., Fouesneau, M., Mantelet, G., & Andrae, R. 2018, AJ, 156, 58
Bailer-Jones, C. A. 2015, PASP, 127, 994
Balaguer-Núnez, L., Tian, K., & Zhao, J. 1998, A&AS, 133, 387
Bate, M. R., Bonnell, I. A., & Bromm, V. 2003, MNRAS, 339, 577
Belwal, K., Bisht, D., Bisht, M. S., et al. 2024, AJ, 167, 188
Belwal, K., Bisht, D., Jiang, I.-G., et al. 2025, MNRAS, 544, 988
Binney, J., & Tremaine, S. 2008, Galactic Dynamics: Second Edition (Princeton Univ. Press)
Bisht, D., Elsanhoury, W., Zhu, Q., et al. 2020, AJ, 160, 119
Bisht, D., Zhu, Q., Yadav, R. K. S., Durgapal, A., & Rangwal, G. 2020, MNRAS, 494, 607
Bohm-Vitense, E., & Canterna, R. 1974, ApJ, 194, 629
Bonatto, C., & Bica, E. 2007, MNRAS, 377, 1301
Bostancı, Z. F., Ak, T., Yontan, T., et al. 2015, MNRAS, 453, 1095
Bovy, J. 2015, ApJS, 216, 29
Bovy, J., & Tremaine, S. 2012, ApJ, 756, 89
Brown, A. G., Vallenari, A., Prusti, T., et al. 2021, A&A, 649, A1
Cantat-Gaudin, T., & Anders, F. 2020, A&A, 633, A99
Cantat-Gaudin, T., Anders, F., Castro-Ginard, A., et al. 2020, A&A, 640, A1
Cantat-Gaudin, T., Jordi, C., Vallenari, A., et al. 2018, A&A, 618, A93
Casado, J. 2021, ARep, 65, 755
Çınar, D. C., Bilir, S., Şahin, T., & Plevne, O. 2025, AJ, 170, 13
Çınar, D. C., Taşdemir, S., Koc, S., & Iyer, S. 2024, PARep, 188, 2
Chambers, K. C., Magnier, E., Metcalfe, N., et al. 2016, arXiv:1612.05560
Chand, T., Sharma, S., Singh, K., et al. 2025, FrASS, 12, 1608196
Chen, X., Wang, S., Deng, L., et al. 2020, ApJS, 249, 18
Corsaro, E., Lee, Y.-N., García, R. A., et al. 2017, NatAs, 1, 0064
Dalessandro, E., Mucciarelli, A., Bellazzini, M., et al. 2018, ApJ, 864, 33
Darma, R., Arifyanto, M., & Kouwenhoven, M. 2021, MNRAS, 506, 4603
De Cat, P. 2007, CoAst, 150, 167
de La Fuente Marcos, R., & de La Fuente Marcos, C. 2009, A&A, 500, L13
de La Fuente Marcos, R., & de La Fuente Marcos, C. 2010, ApJ, 719, 104
Dias, W., Alessi, B., Moitinho, A., & Lépine, J. 2002, A&A, 389, 871
Dias, W. S., Monteiro, H., Moitinho, A., et al. 2021, MNRAS, 504, 356
Elsanhoury, W. H., Haroon, A. A., Elkholy, E. A., Çınar, D. C., et al. 2025, JApA, 46, 21
Gaia Collaboration, Vallenari, A., Brown, A. G. A., et al. 2023, A&A, 674, A1
Gautschy, A., & Saio, H. 1993, MNRAS, 262, 213
Geller, A. M., Mathieu, R. D., Braden, E. K., et al. 2010, AJ, 139, 1383
Girard, T. M., Grundy, W. M., López, C. E., & van Altena, W. F. 1989, AJ, 98, 227
Groenewegen, M. 2021, A&A, 654, A20
Haroon, A. A., Elsanhoury, W. H., Elkholy, E. A., Saad, A. S., & Çınar, D. C. 2025, PhyS, 100, 055006
Haroon, A. A., Elsanhoury, W. H., Saad, A. S., & Elkholy, E. A. 2024, CoSka, 54, 22
Harris, W. E., & Pudritz, R. E. 1994, ApJ, 429, 177
Hasan, P. 2024, BSRSL, 93, 294
Hodapp, K., Kaiser, N., Aussel, H., et al. 2004, AN, 325, 636
Hunt, E. L., & Reffert, S. 2024, A&A, 686, A42
Kharchenko, N., Piskunov, A., Schilbach, E., Roeser, S., & Scholz, R.-D. 2013, A&A, 558, A53
Kharchenko, N., Piskunov, A., Röser, S., Schilbach, E., & Scholz, R.-D. 2005, A&A, 438, 1163
King, I. 1962, AJ, 67, 471
Lada, C. J., & Lada, E. A. 2003, ARA&A, 41, 57
Leroy, A. K., Bolatto, A. D., Ostriker, E. C., et al. 2018, ApJ, 869, 126
Li, Z., & Zhu, Z. 2025, A&A, 700, A280
Lindegren, L., Klioner, S., Hernández, J., et al. 2021, A&A, 649, A2
Liu, L., & Pang, X. 2019, ApJS, 245, 32
Loktin, A. 1997, A&AT, 14, 181
Maciejewski, G., & Niedzielski, A. 2007, A&A, 467, 1065
Marigo, P., Girardi, L., Bressan, A., et al. 2017, ApJ, 835, 77
Mora, M. D., Puzia, T. H., & Chanamé, J. 2019, A&A, 622, A65
Netopil, M., Maitzen, H. M., Paunzen, E., & Claret, A. 2006, A&A, 454, 179
Palma, T., Coenda, V., Baume, G., Feinstein, C., et al. 2025, A&A, 693, A218
Panwar, N., Rishi, C., Sharma, S., et al. 2024, AJ, 168, 89
Pápics, P., Moravveji, E., Aerts, C., et al. 2014, A&A, 570, A8

Pecaut, M. J., & Mamajek, E. E. 2013, ApJS, 208, 9
Piatti, A. 2010, A&A, 513, L13
Piecka, M., & Paunzen, E. 2021, A&A, 649, A54
Prusti, T., de Bruijne, J., Brown, A., et al. 2016, A&A, 595, A1
Rachford, B. L., & Canterna, R. 2000, AJ, 119, 1296
Ricker, G. R., Winn, J. N., Vanderspek, R., et al. 2015, JATIS, 1, 014003
Rojas-Ayala, B., Covey, K. R., Muirhead, P. S., & Lloyd, J. P. 2010, ApJL, 720, L113
Sagar, R., & Joshi, U. 1978, BASI, 6, 37
Salpeter, E. E. 1955, ApJ, 121, 161
Sanders, W. 1971, A&A, 14, 226
Sariya, D. P., Jiang, G., Bisht, D., Yadav, R., & Rangwal, G. 2021, AJ, 161, 102
Sariya, D. P., Jiang, G., Bisht, D., Yadav, R., & Rangwal, G. 2023, NewA, 98, 101938
Schlafly, E., Finkbeiner, D., Jurić, M., et al. 2012, ApJ, 756, 158
Song, F.-F., Niu, H.-B., Esamdin, A., Zhang, Y., & Zeng, X.-Y. 2023, RAA, 23, 095015
Soubiran, C., Cantat-Gaudin, T., Romero-Gómez, M., et al. 2019, A&A, 623, C2
Stubbs, C. W., Doherty, P., Cramer, C., et al. 2010, ApJS, 191, 376
Subramaniam, A., Gorti, U., Sagar, R., & Bhatt, H. C. 1995, A&A, 302, 86
Subramaniam, A., Sahu, D., Sagar, R., & Vijitha, P. 2005, A&A, 440, 511
Taşdemir, S., & Çınar, D. C. 2025, CoSka, 55, 506
Taşdemir, S., Çınar, D. C., Canbay, R., et al. 2025, PARep, 3, 1
TESS Team 2021, TESS Light Curves - All Sectors, STScI/MAST, doi:10.17909/T9-NMC8-F686
Tonry, J., Stubbs, C. W., Lykke, K. R., et al. 2012, ApJ, 750, 99
Vallenari, A., Brown, A. G., Prusti, T., et al. 2023, A&A, 674, A1
van den Bergh, S. 1996, PASP, 108, 986
Vasilevskis, S., Klemola, A., Preston, G., et al. 1958, AJ, 63, 387
Vines, J. I., & Jenkins, J. S. 2022, MNRAS, 513, 2719
Wang, S., & Chen, X. 2019, ApJ, 877, 116
Watson, C. L., Henden, A. A., & Price, A. 2006, SASS, 25, 47
Wright, E. L., Eisenhardt, P. R. M., Mainzer, A. K., et al. 2010, AJ, 140, 1868
Yontan, T., Çakmak, H., Bilir, S., et al. 2022, RMxAA, 58, 333